

A Quiescent Galaxy in a Gas-Rich Cosmic Web Node at $z \sim 3$

Weichen Wang^{1,*}, Sebastiano Cantalupo¹, Marta Galbiati¹, Andrea Travascio^{1,2}, Antonio Pensabene^{1,3,4}, Charles C. Steidel⁵, Gabriele Pezzulli⁶, Bingjie Wang^{7,**}, Xiaohan Wang^{8,1}, Rajeshwari Dutta⁹, Titouan Lazeyras¹, Nicolas Ledos¹, Huiyang Mao^{10,1}, and Giada Quadri¹

¹ Department of Physics, Universita degli Studi di Milano-Bicocca, I-20126 Milano, Italy

² INAF – Osservatorio Astronomico di Trieste, I-34131 Trieste, Italy

³ Cosmic Dawn Center (DAWN), Copenhagen, Denmark

⁴ DTU Space, Technical University of Denmark, DK-2800 Kgs. Lyngby, Denmark

⁵ Cahill Center for Astronomy and Astrophysics, California Institute of Technology, Pasadena, CA 91125, USA

⁶ Kapteyn Astronomical Institute, University of Groningen, NL-9747 AD Groningen, the Netherlands

⁷ Department of Astrophysical Sciences, Princeton University, Princeton, NJ 08544, USA

⁸ Department of Astronomy, Tsinghua University, Beijing 100084, China

⁹ IUCAA, Postbag 4, Ganeshkhind, Pune 411007, Maharashtra, India

¹⁰ Purple Mountain Observatory, Chinese Academy of Sciences, Nanjing 210023, China

January 29, 2026

ABSTRACT

Recent JWST observations have unveiled a large number of quiescent galaxies at $z \gtrsim 3$, bringing potential challenges to current galaxy formation models. Since star formation is expected to be fed by external gas accretion, the knowledge about the circumgalactic media (CGM) of these galaxies is essential to understanding how they quench. In this work, we present the discovery of a massive and passive galaxy ($M_\star \simeq 10^{11} M_\odot$) within the MQN01 structure at $z \simeq 3.25$, containing one of the largest overdensities of galaxies and active galactic nuclei (AGN) found so far at $z \gtrsim 3$. The passive galaxy has a star-formation rate of $4^{+6}_{-2} M_\odot/\text{yr}$, placing it more than 1 dex below the star-forming main sequence, and has no detectable molecular gas ($M_{\text{H}_2} < 7 \times 10^9 M_\odot$). Surprisingly, it is located at the center of a large cool gas reservoir, as traced by bright Ly α and H α emission. By taking advantage of deep multi-wavelength information unique to this field, including deep *Chandra* X-ray data, we argue that the inefficient gas accretion from the CGM onto this galaxy over the last few hundreds of Myr, as suggested by the observations, could be caused by an AGN jet of a nearby star-forming galaxy located at a projected distance of 48 kpc. In particular, we argue that the jet feedback may have maintained a high level of CGM turbulence around the passive galaxy and thus caused a reduced gas accretion over the required time-scales. In addition, the elevated ionizing field provided by the AGN overdensity, including the nearby AGN, can illuminate the passive galaxy's cool CGM and make it visible through fluorescent emission. Our study demonstrates that the star formation rates of high-redshift galaxies could be substantially reduced and maintained at a low level even within gas-rich and overdense environments in particular situations.

Key words. cosmology: large-scale structure of universe – galaxies: evolution – galaxies: high-redshift

1. Introduction

The formation of galaxies is connected to the large-scale cosmic environments they are located in; to put it in a simplified way, galaxies commonly accrete gas from the cosmic web, convert it to stars, and grow in stellar mass since the very early phases of their formation (Blumenthal et al. 1984; Kereš et al. 2005; Tacconi et al. 2020). As such, two key elements of galaxy formation become closely connected to each other, namely the gas in the galaxies' surroundings and the star formation. This whole process, or any individual step of it, may also be slowed down or halted, leading to the emergence of quiescent galaxies (Faber et al. 2007; Man & Belli 2018; Afruni et al. 2019).

The process of converting the gas into the stars appears to be more efficient for galaxies at high redshifts (Noeske et al. 2007; Madau & Dickinson 2014; Förster Schreiber & Wuys 2020) and overdense environments (Steidel et al. 2005; Elbaz et al. 2007; Chiang et al. 2017). Specifically, studies of galaxy proto-clusters or cosmic web nodes at $z \gtrsim 3$ reported that these

environments both host rich reservoirs of cool ($10^4 - 10^5$ K) and molecular gas (e.g., Steidel et al. 2000; Borisova et al. 2016; Cantalupo 2017; Pensabene et al. 2024; Zhou et al. 2025a; see also Pérez-Martínez et al. 2025), different from their local descendants hosting mainly hot gas (Alberts & Noble 2022). Overdense environments at early epochs also see an excess of massive star-forming galaxies with respect to the field (e.g., Elbaz et al. 2007; Hatch et al. 2011; Koyama et al. 2013; Galbiati et al. 2025; Zhou et al. 2025b; Wang et al. 2025a). Therefore, the $z \gtrsim 3$ cosmic web nodes are expected to be the locations where the formation of massive galaxies via gas accretion is exceptionally efficient.

From this perspective, gas-rich cosmic web nodes are uniquely valuable laboratories for investigating which physical processes are most important in facilitating early-phase galaxy formation. As an example study of this kind, a recent work by Wang et al. (2025b) discovered a giant massive star-forming disk forming in such a cosmic web node, suggesting that co-rotating gas inflows could play an important role in the formation of these star-forming systems (see also Venkateshwaran et al. 2024; Jiang et al. 2025; Umehata et al. 2025b; Pensabene et al. 2025).

* e-mail: weichen.wang@unimib.it

** NHFP Hubble Fellow

The emergence of passive galaxies in proto-cluster environments is so far less studied. Recent observations utilizing the James Webb Space Telescope (JWST) or ground-based facilities have made remarkable progress in searching for high-redshift quiescent galaxies in the general field population (e.g., Ilbert et al. 2013; Glazebrook et al. 2017, 2024; D’Eugenio et al. 2020; Valentino et al. 2020; Santini et al. 2021; Nanayakkara et al. 2022; Carnall et al. 2023, 2024; D’Eugenio et al. 2024; Ito et al. 2024; Setton et al. 2024; Baker et al. 2025; de Graaff et al. 2025; de la Vega et al. 2025; Weibel et al. 2025). These studies find abundant massive quiescent systems at $z \gtrsim 3$, with number densities exceeding the predictions from some models or simulations (Valentino et al. 2023; Carnall et al. 2024; Lagos et al. 2025). However, the large-scale environments of these systems remain poorly explored. A few studies suggested that they live in overdense environments based on the number counts of neighbor galaxies (Kubo et al. 2021; Ito et al. 2023; Carnall et al. 2024; Jin et al. 2024; Kakimoto et al. 2024; Tanaka et al. 2024; Alberts et al. 2024; Forrest et al. 2024; de Graaff et al. 2025; McConachie et al. 2025; Witten et al. 2025). On the other hand, observational probes of their circumgalactic medium (CGM) are still scarce (Kalita et al. 2021; Umehata et al. 2025a; Pérez-González et al. 2025; Guo et al. 2025), which however are essential to understanding the regulation of galaxy growth and quenching at high redshifts.

In this work, we present the discovery of a massive quiescent galaxy in a gas-rich environment of a cosmic web node or proto-cluster at $z \sim 3.2$, identified and spectroscopically confirmed from a JWST program. Almost unique with respect to other systems found so far, the cool component of the CGM of this galaxy is visible through fluorescent Ly α emission due to the presence of a large overdensity of AGN in the field (Cantalupo et al. 2005, 2014; Borisova et al. 2016; Travascio et al. 2025). Moreover, deep multi-wavelength datasets are available for this field, including JWST, Hubble Space Telescope (HST), Very Large Telescope (VLT), Atacama Large Millimeter/submillimeter Array (ALMA), and *Chandra*, making it possible to characterize the detailed properties of the gas in and around galaxies. Other identified galaxies of in the structure that are discovered from the NIRSpec observations of the JWST program are all star-forming and are presented in a separate paper (Wang et al. 2025c). In addition, a broader study of photometrically-selected quiescent member galaxies will be presented in a companion paper (M. Galbiati et al. in prep.).

The observations and data reduction are described in Section 2. Measurements of the physical properties of the galaxy are presented in Section 3, with further technical details provided in the appendices. An analysis of the environment of the galaxy is presented in Section 4. Discussions about the implications of the observational results are presented in Section 5. Finally, a short summary is provided in Section 6. A Lambda Cold Dark Matter (Λ CDM) cosmology with $H_0 = 70$ km/s/Mpc, $\Omega_m = 0.3$, and $\Omega_\Lambda = 0.7$ is adopted throughout the paper.

2. Observations and Data Reduction

2.1. Near-infrared and optical imaging

The target galaxy of this work is named MQN01 J004131.9-493704, which we also call the “Red Potato.” It was observed with JWST NIRCam as part of the program GO1835 (F150W2 & F322W2, 1632s; P.I. Cantalupo). In addition, it was also observed with HST as parts of the programs ID 17065 (ACS

F625W & F814W, 10 & 12 orbits; P.I. Cantalupo) and ID 17483 (WFC3 F160W, 1 orbit; P.I. Dutta). Details of the observations and reductions of the NIRCam and ACS images can be found in Wang et al. (2025b). The WFC3 image was reduced with the pipeline CALWF3¹. Additional observations with the VLT HAWKI instrument were conducted in three filters, H, Ks, and the CH4 1.58 μ m narrow filter, as part of the program ID 110.23ZX (P.I. Cantalupo). The exposure time was 1-2 hr for each filter. Details of the data reduction can be found in Wang et al. (2025b) and Galbiati et al. (2025). All images were aligned to *Gaia* astrometry using TWEAKWCS² before being measured for fluxes with SOURCE EXTRACTOR (v. 2.28; Bertin & Arnouts 1996). The point spread function (PSF) profiles for these image filters were made from isolated stars using PHOTUTILS (Bradley et al. 2024).

To prepare for flux measurements in the JWST and HST filters, the images were resampled to the same pixel grid using DRIZZLEPAC (Fruchter & Hook 2002) and PSF-matched using PHOTUTILS. The Source Extractor runs were done in dual mode, using the F322W2 as the detection band as described in Wang et al. (2025b). Flux uncertainties were inferred by placing and measuring flux counts from empty sky apertures with the same area as that used for the galaxy photometry. The images in the HAWKI filters were processed and analyzed in the same way as described above, except that the detection band was made by coadding the H and Ks images.

A total of eight photometric bands are available and included for analysis of this work: three HST filters, ACS/F625W, ACS/F814W, and WFC3/F160W; two JWST/NIRCam filters, F150W2 and F322W2; three VLT/HAWKI filters, CH4, H, and Ks. Along with the ALMA band 6 at observed 1.2 mm (Section 2.3), these filters capture the rest-frame ultraviolet (UV) to near-infrared (IR) part of the galaxy spectral energy distribution (SED) and the potential dust continuum emission.

2.2. Near-infrared and optical spectroscopy

The Red Potato galaxy MQN01 J004131.9-493704 was observed with JWST NIRSpec/MSA as part of the program GO 1835. A filter and grating combination of F170LP/G235H was used, leading to a spectroscopic resolution of $R = 2000$ -3700 in the wavelength range of 1.7-3.2 μ m. The total exposure time on source was 7 hr. More details about the observation setup can be found in Wang et al. (2025b).

Data reduction was conducted using the official jwst pipeline version 1.16.0 and CRDS version jwst_1290.pmap. The Red Potato galaxy shows a bright continuum on the 2D spectrum, the spatial profile of which can be fit with a Gaussian with a width of 1.1 NIRSpec pixel (0.12 arcsec) in standard deviation. A 3- σ spatial window, corresponding to a full width of 7 pixels, was adopted for the galaxy 1D spectrum extraction. The background was measured locally from sky regions in the same slit which are 11-16 pixels away from the galaxy center, and subtracted from the galaxy spectrum. A flux calibration was performed onto the extracted spectrum using the integrated galaxy fluxes measured from the imaging data, in order to correct for the flux loss out of the NIRSpec slit, which is described in Appendix A.

The galaxy redshift is measured to be 3.2496 ± 0.0006 , which is determined by fitting the galaxy stellar continuum using PPXF (Cappellari 2023; Section 3.4). The uncertainty quoted for the redshift is at 2- σ , corresponding to a velocity uncertainty of 40

¹ <https://wfc3tools.readthedocs.io/en/latest/wfc3tools/calwf3.html>

² <https://tweakwcs.readthedocs.io>

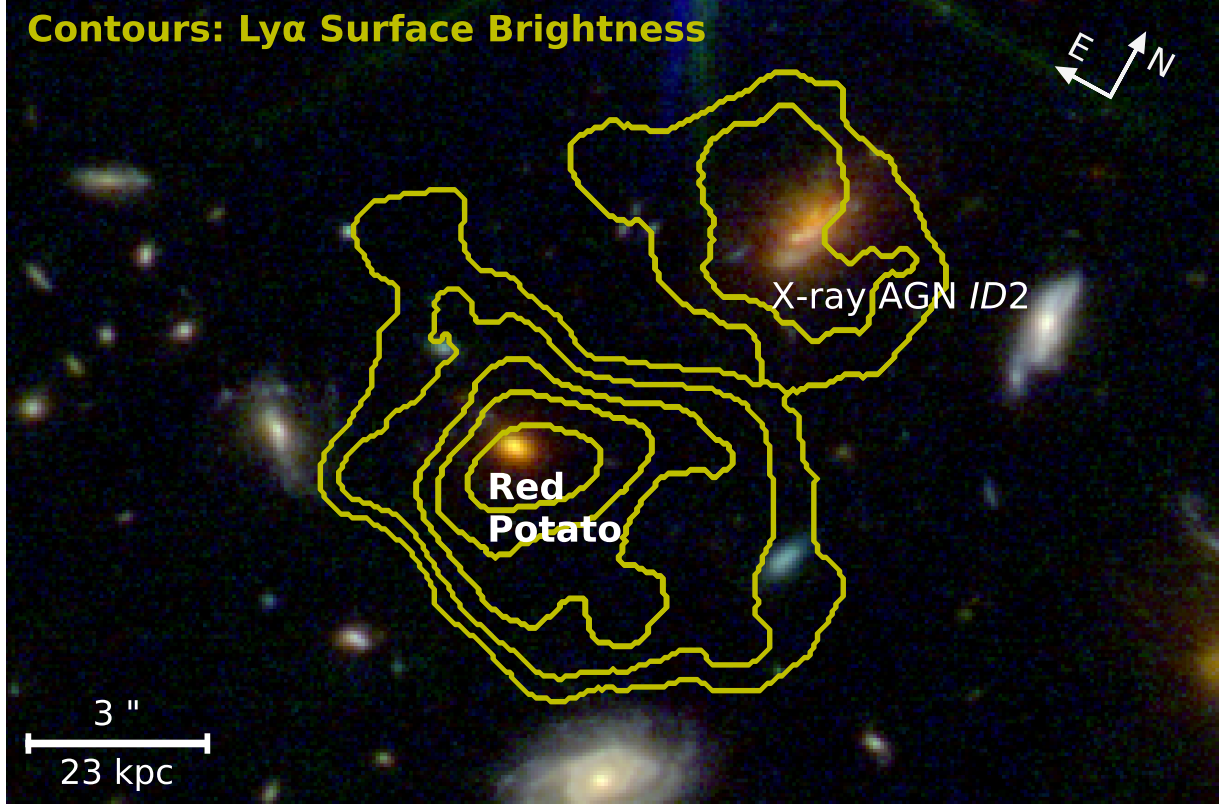


Fig. 1. The passive galaxy MQN01 J004131.9-493704 “Red Potato” at $z=3.250$ and its surrounding cool Ly α -emitting gas reservoir. This massive and compact object was discovered at the center of an extended cool (10^4 – 10^5 K) gas reservoir, as traced by the bright Ly α emission spanning 10 arcsec or 80 kpc (contours) within an overdense region in terms of galaxies and AGN (Pensabene et al. 2024; Galbiati et al. 2025; Travascio et al. 2025). An X-ray bright AGN ID2 from Travascio et al. (2025) was found at a projected distance of only 7 arcsec or 50 kpc and a line-of-sight velocity separation of 100 km/s ($z = 3.251$), likely providing enough ionizing photons to illuminate the CGM of the Red Potato and the CGM of its host galaxy. The color image is made using the NIRCam/F322W2, NIRCam/F150W2, and ACS/F814W for the red, green, and blue channels. The Ly α surface brightness values are $10, 7.0, 5.5, 4.0, 3.0$ ($\times 10^{-18}$ erg/s/cm 2 /arcsec 2) from the outmost to the innermost contour around the Red Potato, and $4.0, 3.0$ ($\times 10^{-18}$ erg/s/cm 2 /arcsec 2) for the contours around the AGN-ID2.

Table 1. Properties of the Red Potato galaxy MQN01 J004131.9-493704

Property	Value	Unit	Reference
Right ascension (J2000)	00h41m31.88s	-	-
Declination (J2000)	-49d37m03.7s	-	-
Redshift	3.2496 ± 0.0006	-	Section 2.2
Stellar mass	$1.1^{+0.4}_{-0.4}$	$10^{11} M_\odot$	Section 3.2
SFR (SED fitting)	4^{+6}_{-2}	M_\odot/yr	Section 3.2
SFR ($H\alpha$)	< 16	M_\odot/yr	Section 3.2
SFR (UV+IR)	< 7 if adopting the SMG template	M_\odot/yr	Section 3.2
Molecular gas mass (M_{H_2})	$< 7 \cdot (\alpha_{\text{CO}}/4 M_\odot \text{ K}^{-1} \text{ km}^{-1} \text{ s pc}^2)$	$10^9 M_\odot$	Section 3.3
Molecular gas fraction (f_{H_2})	$< 0.06 \cdot (\alpha_{\text{CO}}/4)$	-	Section 3.3
Stellar velocity dispersion (integrated)	268 ± 20	km/s	Section 3.4
Half-light radius (along major axis)	1.0 ($1.5 \mu\text{m}$), 0.8 ($3.2 \mu\text{m}$)	kpc	Section 3.5

km/s, and it is calculated by bootstrapping the residual noise in the fitting following Cappellari (2023).

detected with spatially extended Ly α emission, the radial extent of which will be presented in Section 3.

The galaxy and its surrounding field were also observed by the VLT/MUSE with a depth of 10 hours, as part of a Guaranteed Time Observations Program (ID 0102.A-0448; P.I. Cantalupo). Details regarding the observations, data reduction, postprocessing, extraction of the Ly α line emission will be presented in Cantalupo et al. (in prep.; see also Galbiati et al. 2025). The galaxy is

2.3. X-ray, sub-millimeter, and radio observations

The Red Potato galaxy was observed with the *Chandra* Advanced CCD Imaging Spectrometer (Cycle 23, 634 ks; P.I. Cantalupo) and ALMA (Program ID 2021.1.00793.S, 20 hr; P.I. Cantalupo). Details of the observations and data reduction can

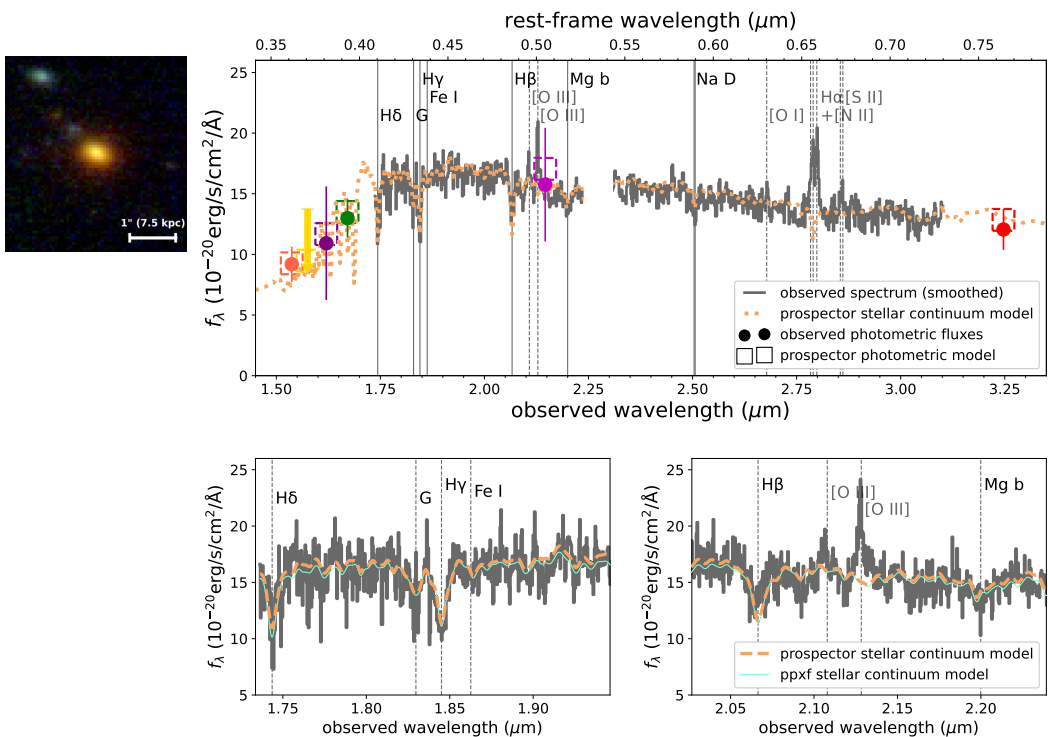


Fig. 2. The spectrum and multi-band photometry suggests the quiescent nature of the Red Potato galaxy. *Top:* The image cutout of the Red Potato galaxy is shown on the left. Its NIRS spectrum, which is smoothed by a 5-pixel box kernel, shows strong Balmer and metal absorption lines (solid vertical lines), suggesting old stellar populations. This is also supported by the D4000 break captured by the multi-band photometry (filled circles). Best-fit models of the stellar continuum and photometric band fluxes from PROSPECTOR are shown as the orange dotted line and open squares, respectively. Nebular emission lines are also present in the observed spectrum, which are however driven by an AGN-like radiation field which we think has an external origin (see Fig. 3 and Section 5.1) rather than be due to internal star formation. A 2σ errorbar is also plotted for each photometric point, except for the case of CH4 where the 2σ upper limit is plotted instead (yellow arrow). *Bottom:* Zoomed-in views of regions where the absorption lines are present, including the H δ , G, Hy, Fe I, H β (blended with a weak emission component), and Mg b lines.

be found in Travascio et al. (2025) and Pensabene et al. (2024), respectively. No significant X-ray detection was found at the location of the galaxy, corresponding to 2σ upper limits of 1.7×10^{-16} erg/s/cm 2 and 2.9×10^{-16} erg/s/cm 2 for 0.5-2 keV and 2-7 keV, respectively (Travascio et al. 2025). Regarding the ALMA observations, the galaxy was not detected with either the 1.2 mm continuum in Band 6 or the CO (4-3) line in Band 3, corresponding to 5σ limits of 0.2 mJy and 2.8×10^9 K km s $^{-1}$ pc 2 (for a velocity window of 300 km/s and the beam size of 1.4''), respectively (Pensabene et al. 2024).

The galaxy was also observed in radio at 0.8 GHz and 1.4 GHz by the Rapid ASKAP Continuum Survey (RACS; McConnell et al. 2020; Hale et al. 2021; Duchesne et al. 2024). The radio images and source flux catalogs were obtained from the ASKAP Science Data Archive³. The RACS maps are known to be subject to astrometric uncertainties of a few arcseconds (McConnell et al. 2020; Duchesne et al. 2024). Thus, we conducted astrometry alignment of the radio images using the bright Quasi-Stellar Object (QSO) of MQN01, CTS G18.01. Specifically, we conducted the alignment by matching the QSO peak locations measured on the ASKAP images to the QSO position measured on the JWST NIRCam image. This leads to an astrometry correction of $\Delta\alpha \cdot \cos\delta = -1.9''$, $\Delta\delta = -1.0''$ for the 0.8 GHz image and a correction of $\Delta\alpha \cdot \cos\delta = -1.6''$, $\Delta\delta = 0.0''$ for the 1.4 GHz image, which are within the ranges of astrometry errors reported in the RACS survey papers (McConnell et al. 2020; Duchesne et al. 2024). The aligned radio maps in both bands can

be found in Appendix C. Details about further analysis of the radio data are deferred to Section 4.3.

3. Analysis of Galaxy Properties

The Red Potato galaxy MQN01 J004131.9-493704 is a massive red system at $z=3.250$ discovered at the center of an extended cool (10^4 - 10^5 K) gas reservoir traced by the Ly α emission, as shown in Fig. 1. Intriguingly, it has a low star formation rate (SFR), at least 1 dex below the star-forming main sequence (SFMS) at its redshift. Detailed physical properties of the galaxy are listed in Table 1, whereas in the following we describe details of the relevant measurements.

3.1. Spectral lines and the full SED

The quiescent nature of the galaxy is first supported by the absorption lines detected in its NIRS spectrum and the shape of its full SED shown in Fig. 2.

The stellar absorption lines indicate old stellar populations formed from a prolonged period of star formation. Specifically, strong Balmer absorption lines (H β , Hy, H δ) and the metal lines (G band 4304Å, Mg b triplet 5175Å, Na D 5894Å) are all present in the NIRS spectrum (Fig. 2). The Balmer lines are contributed by stars with typical ages of several hundred Myr, whereas the G band and Mg b triplet by stars older than 1 Gyr (e.g., Vazdekis et al. 2010). These absorption lines are also commonly found in other high-redshift quiescent systems (Nanayakkara et al. 2022; Glazebrook et al. 2024).

³ <https://research.csiro.au/casda/>

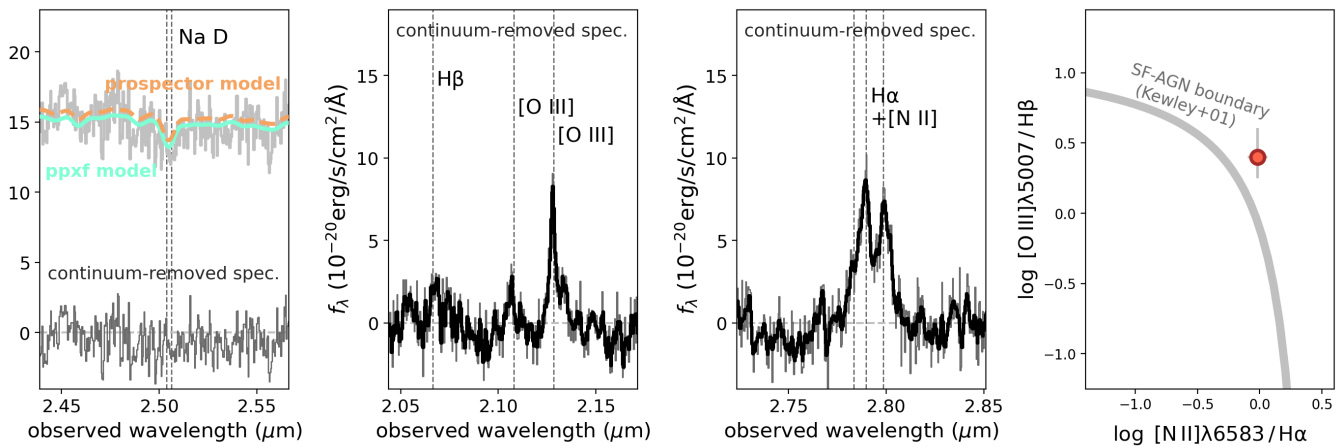


Fig. 3. Profiles of the Na D and nebular lines on the continuum-removed spectrum of the galaxy. *Left panel:* The Na D line profiles before (light gray) and after (black) removing the stellar continuum from PROSPECTOR (orange dashed). The continuum-subtracted spectrum shows no residual absorption component from gas, suggesting the absence of cold ISM gas and outflows. The continuum model from ppxf is also shown (cyan solid) which is consistent with the PROSPECTOR model. *Middle panels:* Hydrogen, [O III], and [N II] lines are detected from the continuum-subtracted spectrum. The black curves represent the spectrum smoothed with a boxcar kernel of 4 pixels and the light gray represent the native-resolution spectrum. *Right panel:* The observed emission lines are driven by an AGN-like spectrum rather than star formation, according to the BPT line ratio criteria by [Kewley et al. \(2001\)](#) and are consistent with the presence of the nearby AGN ID2 or, in general, with an elevated ionizing field produced by the large AGN overdensity in this region

The SED shows a drop below rest-frame $0.4\mu\text{m}$ according to the broadband photometry, which is plotted as filled circles in Fig. 2. This indicates a significant D4000 break and hence the presence of old stellar populations. The filter names of the photometric measurements can be found later in Fig. 4.

A few nebular emission lines are also detected in the galaxy spectrum, including the [O III] 4959Å, [O III] 5007Å, H α , and the [N II] 6548/6583Å doublet, as shown in Fig. 3. However, an analysis of the line flux ratios, described in the following Section 3.2, indicates that they are produced by an AGN-like spectrum rather than by ongoing star formation.

3.2. Stellar mass, SFR, and AGN activity

The galaxy is a massive quiescent system at least one order of magnitude below the SFMS at its epoch, according to its stellar mass and SFR values inferred from the observed photometric fluxes and spectrum. The fluxes and spectrum, along with a best-fit model spectrum obtained using the PROSPECTOR code ([Leja et al. 2017](#); [Johnson et al. 2021](#); [Wang et al. 2024](#)), are presented in Figs. 2 & 4.

The PROSPECTOR fitting was done simultaneously onto the observed photometric fluxes in eight filters from optical to near-infrared (Section 2.1) and the NIRSpec spectrum. A non-parametric star formation history (SFH) was adopted, with a prior favoring constant star formation and continuity as described in [Leja et al. \(2019\)](#) and eight lookback time bins of 0-10 Myr, 10-100 Myr, 100-200 Myr, 200-350 Myr, 350-550 Myr, 550-800 Myr, 800-1200 Myr, and 1200-1930 Myr. A [Chabrier \(2003\)](#) initial mass function and a flexible dust attenuation law by [Charlot & Fall \(2000\)](#) were adopted. The stellar metallicity was set as a free parameter with a flat prior. The Balmer, [N II], and [O III] emission lines were fit with standalone Gaussians and their contributions to the broadband fluxes are taken into account in the SED fitting. However, because these lines are driven by AGNs as shown below, they were neglected for the step of modeling the SFH and stellar populations in the PROSPEC-

TOR fitting (see also, e.g., [de Graaff et al. 2025](#) for a similar treatment). The model spectrum was smoothed by the instrument line spread function and a Gaussian with the same width as the measured stellar velocity dispersion (Section 3.4) before being fit to the NIRSpec data. Following the practices adopted by studies involving fitting the galaxy NIRSpec spectra with PROSPECTOR (e.g., [Beverage et al. 2025](#); [de Graaff et al. 2025](#)) and other tools (e.g., [Cappellari 2023](#); [Scholtz et al. 2024](#)), the smooth large-scale variation of the spectrum was modeled as a multiplicative polynomial of 11th order in the fitting run. Other details of the fitting setup are similar to what discussed in [Wang et al. \(2024\)](#). A galaxy SED model was generated from the best-fit parameters and shown in Figs. 2 & 4, along with the best-fit SFH in the right panel of Fig. 4.

The Red Potato galaxy is a massive system with a stellar mass of $1.1_{-0.4}^{+0.4} \times 10^{11} M_{\odot}$ and a SFR of $4_{-2}^{+6} M_{\odot}/\text{yr}$ (100-Myr timescale) according to the fitting results, where the quoted errors include both the $1-\sigma$ statistical uncertainties measured from the fitting posteriors and the systematic errors quantified by [Pacifici et al. \(2023\)](#). As shown in the middle panel of Fig. 5, the measured stellar mass and SFR values place the galaxy more than 1 dex below the SFMSs reported by the literature ([Popesso et al. 2023](#); [Speagle et al. 2014](#)). Other massive ($> 10^{10} M_{\odot}$) galaxies discovered in the same proto-cluster MQN01 from [Galbiati et al. \(2025\)](#) and [Pensabene et al. \(2025\)](#) are also shown in the panel for comparison, which are all located around the main sequence. These objects include the host galaxy of the AGN-ID2 shown in Fig. 1 at $10^{11.2} M_{\odot}$, the Big Wheel galaxy from [Wang et al. \(2025b\)](#) at $10^{11.4} M_{\odot}$, and the QSO companion galaxy from [Pensabene et al. \(2025\)](#) at $10^{11.0} M_{\odot}$.

We also tested whether the SED fitting results are robust against the choice of SFH. Specifically, we switched to a parametric SFH, the delayed exponentially-declining form $\text{SFR}(t) \propto t \cdot e^{-t/\tau}$, and repeated the fitting with identical setups as above for all other parameters. The inferred mass and SFR values are $1.1_{-0.4}^{+0.5} \times 10^{11} M_{\odot}$ and $7_{-4}^{+7} M_{\odot}/\text{yr}$, respectively, consistent with those inferred from the fitting with a non-parametric SFH if taking into account the uncertainties.

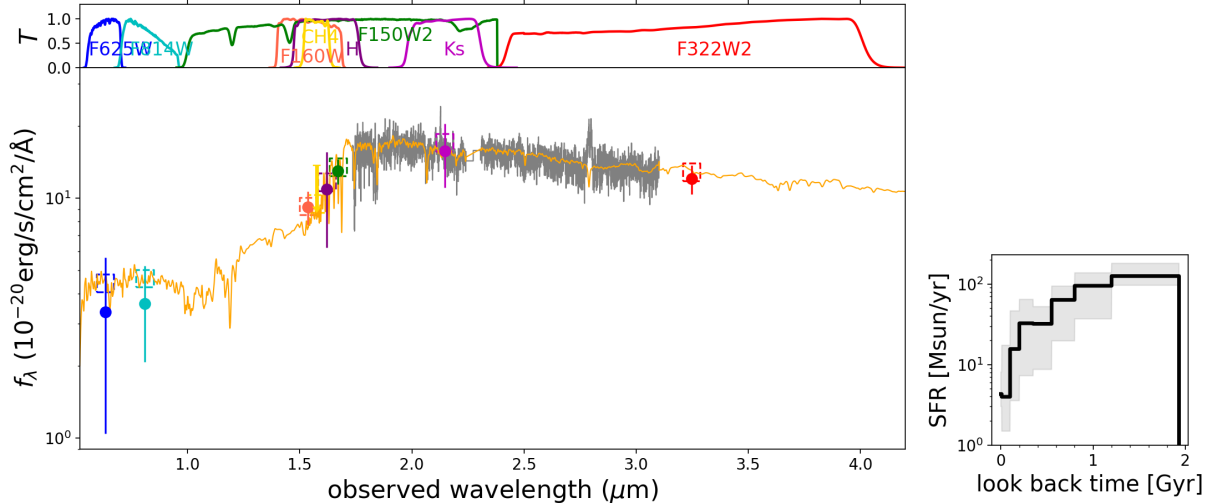


Fig. 4. The full galaxy SED measured from the NIRSpec spectroscopy (gray curve) and multi-band photometry (filled circles), and the corresponding models from PROSPECTOR (orange curve and open squares) are shown in the left panel. The PROSPECTOR fitting results suggest a SFR below $10 M_{\odot}/\text{yr}$, demonstrated by the best-fit SFH in the right panel, corresponding to $\text{ssFR} < 10^{-10} \text{ yr}^{-1}$. The low SFR is also supported by the faint rest-frame UV fluxes (F625W and F814W filters) and the non-detection of dust continuum emission from ALMA (not shown in figure). During the PROSPECTOR fitting, the observed emission lines were neglected in the step of modeling the stellar population and SFH, considering that these lines are likely not produced by internal star formation (Fig. 3). The transmission curve of each photometric filter is also shown at the top.

In addition to the SED fitting, the low SFR of the galaxy is also supported by measurements of the Balmer lines and the dust continuum emission. The $\text{H}\alpha$ line flux measured from the continuum-subtracted spectrum is $5.6 \pm 0.4 \times 10^{-18} \text{ erg/s/cm}^2$ in the rest frame. If the line were entirely powered by star formation, we can infer from the flux the SFR (10-Myr timescale) to be $2.8 \pm 0.2 M_{\odot}/\text{yr}$, following Kennicutt & Evans (2012). If assuming a Calzetti (2001) dust law, we infer the $\text{H}\alpha$ dust attenuation to be 0.5 mag with a 2- σ upper limit of 1.8 mag from the $\text{H}\alpha/\text{H}\beta$ line ratio. Adopting this limit value, the corresponding 2- σ upper limit of the total SFR is $16 M_{\odot}/\text{yr}$. We stress that these are highly conservative upper limits, given the presence of AGN radiation. The SFR limit can also be evaluated from ALMA observations of the dust continuum, in which the galaxy is not detected at 1.2 mm. Following Santini et al. (2019) and including the UV SFR measured from the HST F625W flux, this leads to a 2- σ upper limit of $7 M_{\odot}/\text{yr}$ for the total SFR if adopting the dust SED templates of high-redshift sub-millimeter galaxies (SMGs) by Michałowski et al. (2010), where the dust temperature is assumed to be around 40 K. Both of the SFR upper limits calculated above are consistent with the value from SED fitting and indicated in Fig. 5.

The galaxy nebular line emission is due to AGN radiation according to the BPT diagram criteria (Baldwin et al. 1981; Kewley et al. 2001), demonstrated by the galaxy-integrated measurements in Fig. 3 (right panel). The emission line fluxes are measured from the continuum-subtracted NIRSpec spectrum. We discuss the origin of the AGN-type radiation in Section 5.

3.3. Low cold gas fraction traced by CO & Na D

The Red Potato galaxy is not detected in CO(4-3) line emission by deep ALMA observations, which can be used to put an upper limit on its cold molecular gas mass (M_{H_2}). We calculate this upper limit using the sensitivity of the CO(4-3) line flux measurement (table 4 in Pensabene et al. 2024) and a CO line ratio $r_{41} = L'(\text{CO 4-3})/L'(\text{CO 1-0}) = 0.61 \pm 0.13$ as adopted by Boogaard et al. (2020) and Pensabene et al. (2024). The in-

ferred 2- σ upper limit of M_{H_2} is $7(1.4) \times 10^9 M_{\odot}$ if assuming $\alpha_{\text{CO}} = 4(0.8) M_{\odot} \text{ K}^{-1} \text{ km}^{-1} \text{ s pc}^2$ (see Bolatto et al. 2013). Such a limit corresponds to a 2- σ limit $f_{\text{H}_2} = M_{\text{H}_2}/(M_{\star} + M_{\text{H}_2})$ of only 0.06 (0.01) for the molecular gas fraction.

These constraints indicate that the galaxy is a molecular gas-poor system: as demonstrated in the right panel of Fig. 5, its molecular gas fraction is around ten times lower than those of typical field star-forming galaxies at similar masses and redshifts measured by Tacconi et al. (2018), and yet rather consistent with recent measurements of $z \sim 3$ quiescent galaxies (Magdis et al. 2021; Scholtz et al. 2024; Umehata et al. 2025a). The gas-poor nature of the galaxy is also corroborated by the non-detection of the Na D line absorption tracing the cold atomic gas ($\lesssim 10^3 \text{ K}$; Veilleux et al. 2005) of the interstellar medium (ISM), which is shown in the left panel of Fig. 3 and described in Section 3.4.

3.4. Stellar kinematics & the non-detection of cold outflows

The stellar kinematics of the galaxy are modeled by fitting the integrated galaxy spectrum with the ppxf code (Cappellari 2023). Stellar population synthesis models from the Flexible Stellar Population Synthesis (FSPS; Conroy et al. 2009; Conroy & Gunn 2010) are adopted, and the NIRSpec instrument line spread function is taken into account. Shown as the cyan curve in the lower panels of Fig. 2, the best-fit spectrum (excluding emission line components) reproduces the strong absorption features as observed and is consistent with the model spectrum from PROSPECTOR (orange dashed curve therein).

The intrinsic stellar velocity dispersion integrated over the whole galaxy is measured to be $268 \pm 20 \text{ km/s}$, which is typical of high-redshift quiescent galaxies at stellar masses of around $10^{11} M_{\odot}$ (van de Sande et al. 2013; Forrest et al. 2022; Kriek et al. 2024). We defer the analysis of the ionized gas kinematics to Section 4.1.

The same steps of ppxf fitting are also applied to the spectra of individual regions in cases where the spectral continuum emission is detected. The resulting continuum-subtracted spectra are used for the emission line analysis in Section 4.1.

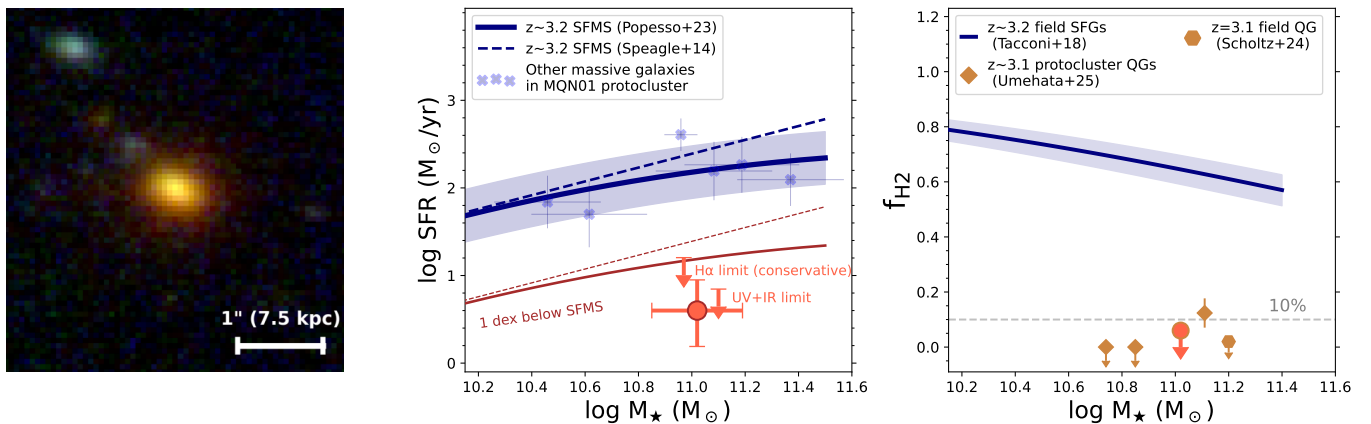


Fig. 5. Morphology and physical properties of the Red Potato galaxy, which is marked by large red circles in the middle and right panels. *Left:* The galaxy has a red and compact morphology in the JWST+HST color image. *Middle:* It is a massive system with $M_{\star} \simeq 10^{11} M_{\odot}$ and at least one dex below the main sequence at its redshift of $z=3.250$ (blue curves; Speagle et al. 2014; Popesso et al. 2023), according to the SED fitting and the SFR upper limits from UV+IR and H α (red downward arrows). Its SFR is also substantially lower than those of other massive galaxies discovered in the same proto-cluster MQN01 (light blue squares; see Galbiati et al. 2025; Pensabene et al. 2025 and main text). *Right:* The galaxy is poor in molecular gas, with a gas fraction $f_{H_2} \lesssim 0.06$, substantially smaller than those of the field star-forming galaxies (SFGs, solid curve; Tacconi et al. 2018). Similarly low fractions, smaller than around 10%, are also found in other massive $z \sim 3$ quiescent galaxies (Scholtz et al. 2024; Umehata et al. 2025a).

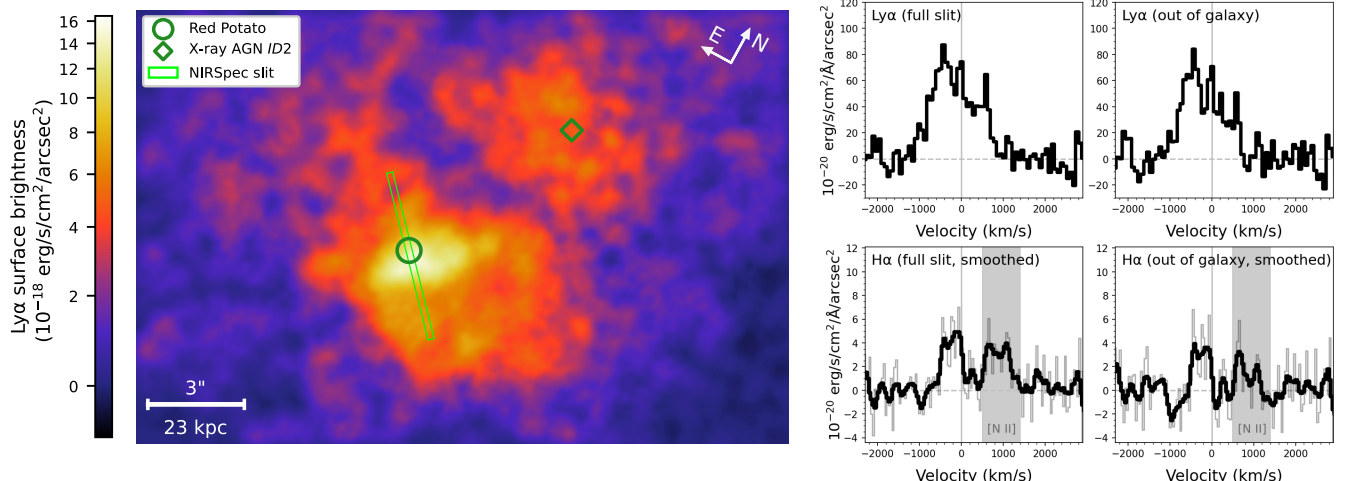


Fig. 6. The Ly α surface brightness map and the emission line profiles extracted from the NIRSpec slit, which indicate the presence of an extended cool CGM gas reservoir around the Red Potato. *Left panel:* The Ly α map from MUSE (smoothed) overlaid with the NIRSpec slit footprint. The Ly α emission is spatially extended with a bright, elongated core reaching a few times $10^{-17} \text{ erg/s/cm}^2/\text{arcsec}^2$. *Middle panels:* The Ly α (top) and H α (bottom) line profiles extracted from the spatial region covered by the slit. The H α line profile at the native spectral resolution is shown in light gray and the profile after smoothing with a boxcar filter of 4 pixels is shown in black. The gray shade marks the region which could be affected by the [N II] 6583Å line. *Right panels:* Similar to the middle panels but the spectra are extracted from the slit region away from the galaxy, namely at distances more than $0.35''$ from the galaxy center which is the slit area not enclosed by the open circle symbol in the left panel. The Ly α /H α ratio measured from the middle panels is $6.8^{+1.5}_{-1.0}$ and that from the right panels is $9.8^{+4.8}_{-2.5}$, excluding the region affected by the [N II] 6583Å line. These values are both consistent with the recombination emission mechanism considering the possible effect of local Ly α scattering (Langen et al. 2023). Both the Ly α and H α spectral profile appears relatively broad or present multiple possible components, suggesting complex kinematics and/or a turbulent medium.

No molecular and cold atomic gas outflows are detected from the galaxy. The two gas phases are traced by the CO line and Na D doublet lines, respectively. The non-detection of the molecular gas is naturally justified by the non-detection of the CO line (Section 3.3). Constraints on the neutral outflow are demonstrated in the left panel of Fig. 3, showing that after removing the best-fit stellar continuum from PROSPECTOR (orange dashed line) the NIRSpec spectrum (black line) does not show any residual absorption of Na D. The same finding is reached if using alternatively the best-fit stellar continuum from ppxf (cyan line);

masking out the Na D line region or not in the fitting leads to identical results. These analyses suggest that there exists no extra component of Na D absorption from either the ISM gas or outflows.

The molecular and neutral phases are reported to dominate the mass budget of the AGN- or star formation-driven outflows from typical massive galaxies (Roberts-Borsani 2020; Avery et al. 2022; Baron et al. 2022; Belli et al. 2024). Hence the absence of these mass-loaded outflows from the Red Potato suggests that there is no substantial ejective feedback. In com-

parison, strong neutral outflows traced by optical/UV absorption lines have been observed in several other $z > 3$ massive quiescent galaxies (e.g., Man et al. 2021; D’Eugenio et al. 2024; Scholtz et al. 2024; Valentino et al. 2025; Wu 2025; see also Belli et al. 2024), likely suggesting that they are at a quenching stage earlier than the Red Potato (Park et al. 2024).

3.5. Galaxy morphology

In terms of morphology, the galaxy appears as a red and compact spheroid as shown in the left panel of Fig. 5. The image was created using the F322W2 (3.2 μm), F150W2 (1.5 μm), and F814W (0.8 μm) filters for the R, G, B channels, respectively. We also analyzed the morphology quantitatively by fitting the NIRCam images with Sérsic profiles (Sérsic 1963) using the PYSERIC code (Pasha & Miller 2023), which is demonstrated in Appendix B. The galaxy is best fit with a half-light radius of 0.13 and 0.11 arcsec and a Sérsic index of 1.5 and 2.6 for the F150W2 and F322W2 filters, respectively. The galaxy half-light radius in the rest-frame optical (0.5 μm) can be inferred by interpolating between the F150W2 and F322W2 sizes (Wang et al. 2025b). The inferred radius is 0.9 kpc, which is consistent with those of the field quiescent galaxies at similar masses and redshifts and substantially smaller than those of star-forming galaxies (Baker et al. 2025; Kawinwanichakij et al. 2025; Yang et al. 2025). The Sérsic index values (1.5, 2.6) are smaller than the typical value of 4 as found for the local early-type galaxies (e.g., Gadotti 2009). Sérsic indices lower than 4 are also reported among other quiescent galaxies discovered at $z > 3$, indicating a probable evolutionary connection with disk galaxies at even earlier epochs (e.g., Man et al. 2021; Carnall et al. 2023, 2024; Glazebrook et al. 2024; Ito et al. 2024; Sato et al. 2024; Setton et al. 2024; Baker et al. 2025; Kawinwanichakij et al. 2025).

4. Analysis of the CGM & Environment

4.1. Detection of an extended reservoir of cool gas from the $\text{Ly}\alpha$, $\text{H}\alpha$, & $[\text{O III}]$ emission lines

Extended $\text{Ly}\alpha$ emission has been found around the Red Potato, indicating the presence of an extended reservoir of cool gas, which is also shown by the $\text{Ly}\alpha$ map in Figs. 1 & 6. This discovery is corroborated by further measurements of the $\text{Ly}\alpha$, $\text{H}\alpha$, and $[\text{O III}]$ lines. We present these measurements and an analysis of the physical origin of the line emission in the following.

The $\text{Ly}\alpha$ surface brightness map around the Red Potato galaxy is shown in Fig. 6. The $\text{Ly}\alpha$ emission is spatially extended and bright, reaching a surface brightness of a few times $10^{-17} \text{ erg/s/cm}^2/\text{arcsec}^2$ in the center. The two upper right panels show the $\text{Ly}\alpha$ spectra extracted from a pseudo-slit of the MUSE dataset matched to the NIRSpec slit, and the two bottom right panels show the $\text{H}\alpha$ spectra extracted from the NIRSpec slit.

The $\text{Ly}\alpha/\text{H}\alpha$ line flux ratio measured from the full slit is $6.8^{+1.5}_{-1.0}$. If excluding the galaxy region, namely within 0.35'' from the galaxy center, the line ratio measured from outside of the galaxy is $9.8^{+4.8}_{-2.5}$. For $\text{Ly}\alpha$, the line flux is measured from a velocity window of [-1500, 1500] km/s considering the broad line profile seen in Fig. 6. For $\text{H}\alpha$, the flux is measured from a velocity window of [-500, 500] km/s, which excludes the region that could be contaminated by the $[\text{N II}]$ 6583Å line, as marked in the figure. The $\text{H}\alpha$ can be subject to blending with the nearby $[\text{N II}]$ 6548Å line, which is three times weaker than the $[\text{N II}]$ 6583Å line. To assess the impact of the line blending,

we scaled down the emission within the $[\text{N II}]$ 6583Å region by a factor of 3, shifted it to the location of the $[\text{N II}]$ 6548Å, and subtracted it from the observed spectrum before measuring the $\text{H}\alpha$ line flux. The resulting $\text{H}\alpha$ line flux is measured to be $2.25 \pm 0.41 \times 10^{-18} \text{ erg/s/cm}^2/\text{arcsec}^2$, which only decreased by 9% compared to the original value of $2.38 \pm 0.41 \times 10^{-18} \text{ erg/s/cm}^2/\text{arcsec}^2$, indicating no substantial impact of possible line blending on the $\text{H}\alpha$ flux measurement.

The high surface brightness of the extended $\text{Ly}\alpha$ and the measured $\text{Ly}\alpha/\text{H}\alpha$ ratios support a scenario for which the emission lines are produced by recombination radiation of a highly clumpy medium in and around the galaxy (e.g., Cantalupo et al. 2014, 2019; Leibler et al. 2018; Langen et al. 2023).

We also present the 2D spectra of $\text{H}\alpha$ and $[\text{O III}]$ 5007Å and show that they extend beyond the galaxy in Fig. 7. The slit footprint is shown in the left panel and aligned with the 2D spectra along the Y axis. Both lines extend beyond the NIRSpec continuum (Section 2.2), which is marked by the horizontal dashed lines. Specifically, the $\text{H}\alpha$ and $[\text{O III}]$ lines reach as far as 1 arcsec or 8 kpc above (i.e., north to) the galaxy center. Tentative $\text{H}\alpha$ detection is also found below the galaxy.

4.2. Detailed analysis of CGM spatial extent and kinematics

We present detailed analysis of the spatial extent of the emission lines and gas kinematics in Figs. 8 & 9 and show that the emission lines tracing Red Potato’s CGM have broad profiles, corresponding to high velocity dispersion. Relevant implications on the CGM turbulence will be discussed later in Section 5.

Regarding the spatial extent, the $\text{Ly}\alpha$ emission around the Red Potato galaxy is found to reach over 50 kpc in radial distance, which is shown in the left panel of Fig. 8. The $\text{Ly}\alpha$ emission is also remarkably bright, only slightly fainter than the average profile of the $\text{Ly}\alpha$ nebulae around bright $z \sim 3$ QSOs measured by Borisova et al. (2016) (black curve; $i_{\text{QSO}} < 19$ mag) and brighter than those of faint $z \sim 3$ QSOs measured by Mackenzie et al. (2021) (green curve; $i_{\text{QSO}} \gtrsim 20$ mag). Red Potato’s $\text{Ly}\alpha$ surface brightness profile is also flatter than the QSO profiles at $r \gtrsim 30$ kpc due to the contribution of $\text{Ly}\alpha$ emission around the nearby AGN-ID2, whose location is marked with the orange arrow in the figure.

The spatial extents measured from $\text{H}\alpha$ and $[\text{O III}]$ lines along the NIRSpec slit are also shown in Fig. 8 (right panel). The $\text{H}\alpha$ and $[\text{O III}]$ flux profiles (red and blue curves) are both more extended than the galaxy continuum (gray curve). The $\text{H}\alpha$ appears more extended than the $[\text{O III}]$ towards the upward direction along the slit, indicating that the former might be the better tracer of the large-scale CGM for the case of the Red Potato.

Regarding the gas kinematics, the $\text{Ly}\alpha$ velocity dispersion of Red Potato’s inner CGM ($20 \text{ kpc} \lesssim r \lesssim 30 \text{ kpc}$) is found to be 400–500 km/s, which is significantly higher than those measured from the $z \sim 3$ QSOs with comparable $\text{Ly}\alpha$ surface brightness at the same distances, which are around 50–200 km/s. This is demonstrated in the middle panel of Fig. 8. The QSO nebula profiles for comparison are from two subsamples in a study by González Lobos et al. (2025) which bracket the $\text{Ly}\alpha$ surface brightness profile of Red Potato’s inner CGM, as shown in the left panel. Specifically, these two subsamples are the first and fourth bins listed in the top panel of tab. 3 of the paper. The $\text{Ly}\alpha$ velocity dispersion values are all measured from the second moment of the line spectral profile, which is the common practice among the literature (e.g., Borisova et al. 2016). We note that multiple spatial components oriented along our line of sight

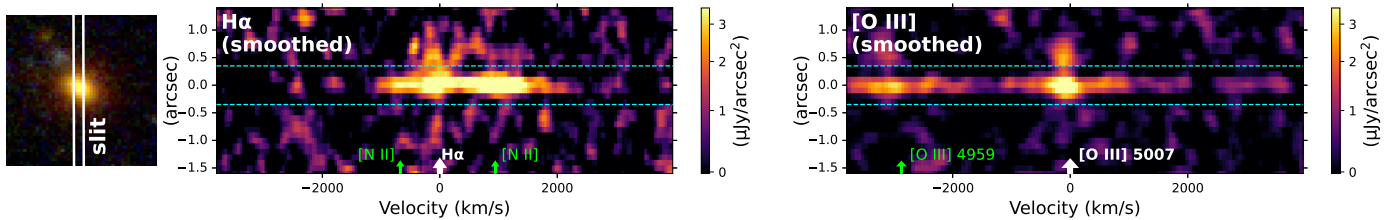


Fig. 7. The 2D spectra of H α and [O III] 5007 \AA lines tracing the extended cool ionized gas around the Red Potato. *Left*: The NIRSpec slit footprint from where the 2D spectra are extracted. *Middle and Right*: The 2D spectra of H α and [O III]. Both spectra are aligned spatially with the slit image along the Y axis (in unit of arcsec), and the galaxy spatial extent and locations of the nearby emission lines are all marked in each panel. Both emission lines extend beyond the galaxy spatial extent along the slit. The spectra are smoothed along the Y direction to a spatial resolution of 0.7'' (FWHM), and along the X axis with a boxcar filter of 4 and 3 pixels for H α and [O III], respectively, corresponding to 200 km/s. The continuum has been removed through a row-by-row median filtering.

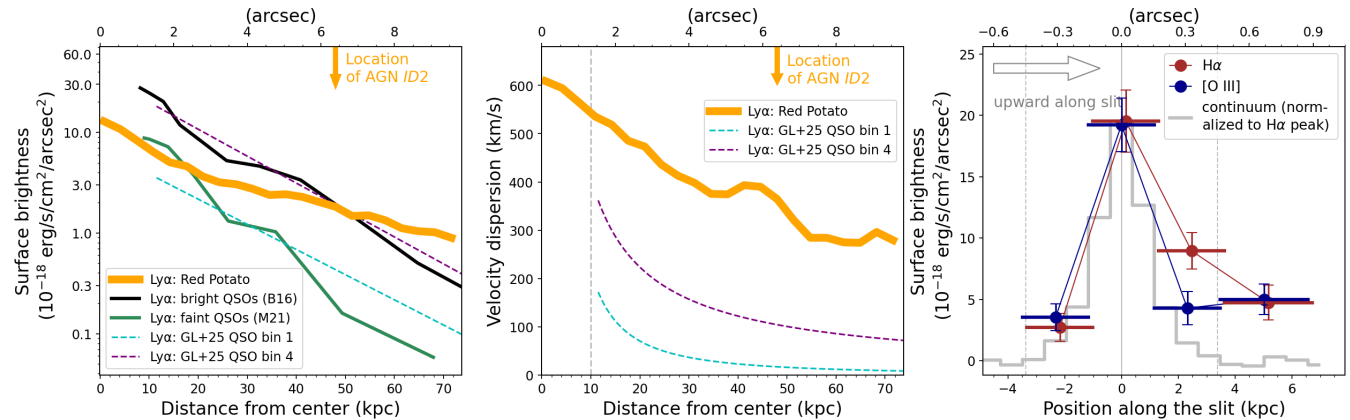


Fig. 8. The spatial extent and kinematics of Red Potato's CGM measured from emission lines. *Left*: Radial Ly α surface brightness profile measured around the Red Potato (orange curve). The Ly α emission is remarkably bright and comparable to those of bright QSOs at $z \sim 3$. The black curve represents the median profile of the Ly α nebulae around bright $z \sim 3$ QSOs from Borisova et al. (2016) and the green curve represents the profile for faint $z \sim 3$ QSOs from Mackenzie et al. (2021). Red Potato's profile is flatter than the QSO profiles at $r \gtrsim 30$ kpc, possibly due to the contribution of Ly α emission around the nearby AGN-ID2, whose location is marked with the orange arrow. The dashed lines represent the best-fit profiles for two subsamples of $z \sim 3$ QSO nebulae from González Lobos et al. (2025) which bracket Red Potato's profile at $r < 30$ kpc. The QSO Ly α surface brightness values are all adjusted to Red Potato's redshift. *Middle*: The Ly α velocity dispersion profile measured around the Red Potato (orange curve). Measurements for the two subsamples of González Lobos et al. (2025) are shown for comparison (dashed lines). Red Potato's CGM has substantially higher Ly α velocity dispersion than the two subsamples at $20 \text{ kpc} \lesssim r \lesssim 30 \text{ kpc}$. *Right*: Surface brightness of H α and [O III] 5007 \AA measured along the NIRSpec slit. The emission lines are more extended than the continuum (gray) along the slit. The continuum is normalized to the H α profile peak.

could also result in apparently large velocity dispersion. However, we have no indications from the galaxy spatial and redshift distribution that this could be the case, although deeper JWST data would be needed to fully exclude this hypothesis.

We investigate the gas kinematics further using the 1D spectra of the H α and [O III] lines, which are shown in Fig. 9. The spectra are extracted from spatial regions inside the galaxy (middle panels) and around the galaxy (left and right panels). The H α and [O III] lines are detected in the regions above and within the galaxy (left and middle panels), and the results of Gaussian fitting to the line profiles are also shown. Tentative detection of the H α is also found in the region below the galaxy.

In the region above the galaxy, both the H α and [O III] lines are detected with velocity dispersion (σ ; corrected for instrument line spread function) above 100 km/s. In addition, the H α line profile measured from this region appears broad and complex (upper right panel), which we discuss further in Section 5.

The gas velocity dispersion measured from the H α line *within* the Red Potato galaxy is around 200 km/s, which is two or three times the typical values measured from SFGs at similar masses and redshifts (Simons et al. 2017; Danhaive et al. 2025; Wisnioski et al. 2025), and no significant velocity gradi-

ent is found across the galaxy. This indicates the presence of dispersion-dominated gas in the Red Potato galaxy. In other words, the Red Potato appears to be a dispersion-dominated system according to the the H α kinematics, whereas some other high-redshift quiescent galaxies are found to be rotation-dominated (e.g., D'Eugenio et al. 2024).

The Ly α line profiles are also shown in the bottom panels of Fig. 9 for reference. They are extracted from spatial regions four times wider than the NIRSpec slit area to ensure sufficient signal-to-noise. However, we note that a quantitative comparison between the Ly α and H α lines cannot be performed within these apertures, which are still not large enough to mitigate the impacts of seeing and possible local resonant scattering on the Ly α .

4.3. The nearby X-ray AGN and evidence for a jet

As shown in Figs. 1 & 10, the Red Potato galaxy is found close to another galaxy which is at a similar redshift of $z = 3.251$ (versus $z = 3.250$ for the Red Potato) and hosts a luminous X-ray AGN (Pensabene et al. 2024; Galbiati et al. 2025; Travascio et al. 2025). The X-ray source, identified and named as *ID2* in Travascio et al. (2025), is located at a projected dis-

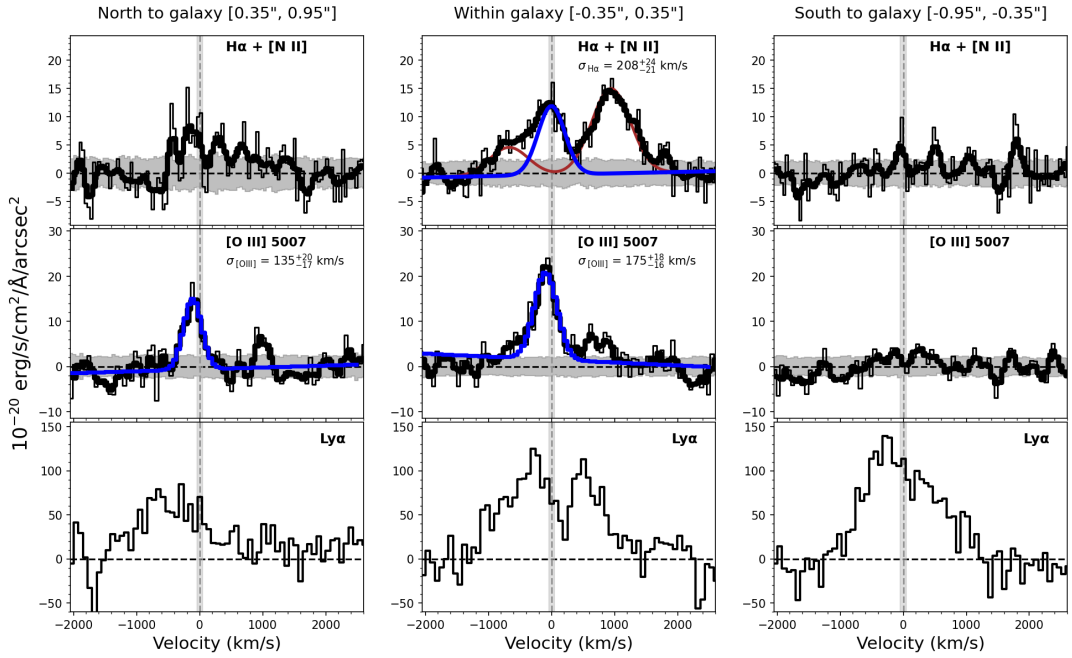


Fig. 9. The 1D spectra of the H α (top row) and [O III] 5007 Å (middle row) extracted from regions in and around the Red Potato along the NIRSpec slit. The Ly α spectra extracted from a wider area around the NIRSpec slit are also presented in the bottom panel for a qualitative comparison (see text for details). From left to right, the spectra are extracted from above (north to), within, and below (south to) the galaxy (c.f. Fig. 7), respectively. The thin gray lines represent the profiles at the native resolution and the thick black lines represent the smoothed profiles. The H α and [O III] lines are detected in the regions above and within the galaxy. Tentative detection of the H α is also found south to the galaxy. The blue curves represent Gaussian profile fitting models of the H α and [O III] lines, when possible. The brown curve represents the fit to the [N II] lines. The velocities are all with reference to the galaxy systemic redshift, the 2- σ uncertainty range of which is indicated by the vertical shades. The standard errors of the NIRSpec spectra are indicated as the light gray shades in the top and middle panels. Especially in the northern region, which is the area closer to the X-ray jet detection (see Fig. 10), the H α spectrum appears kinematically complex as shown in the top left panel.

tance of 6.4 arcsec or 48 kpc and has a luminosity of $L_{2-10 \text{ keV}} = 10^{45}$ erg/s, making it the brightest X-ray source of the MQN01 structure after the central QSO of MQN01.

As also shown in the left panel of Fig. 10, the Red Potato galaxy position, as well as the AGN-ID2, is within the 20"-wide ASKAP beam of a radio source detected at 0.8 GHz, indicating a certain form of radio AGN feedback in action. The source has a measured flux of 1.56 ± 0.47 mJy, the brightest of the large-scale structure. There is no detection at 1.4 GHz, corresponding to a 2- σ flux upper limit of 0.36 mJy (Duchesne et al. 2024). From the 0.8 GHz and 1.4 GHz measurements, a radio spectral index α , defined as $S \propto \nu^{-\alpha}$ where S is the flux density and ν is the frequency, can be determined. The inferred α is above 2.8 at 2- σ significance. Such a steep spectral index can be produced by an aged radio jet (Myers & Spangler 1985; Alexander & Leahy 1987; Brienza et al. 2021).

The right panel of Fig. 10 shows the X-ray count map zoomed into a smaller sky region. Intriguingly, the X-ray emission is found extended over about 40 kpc, which is marked by the pink box in the figure, and the extended emission is approximately aligned in the direction from the AGN-ID2 to the Red Potato. Such emission is indicative of an AGN jet, which most likely emanates from the AGN-ID2 since the extended emission appears connected to the AGN-ID2 itself on the X-ray image. This jet is most likely the cause of the radio emission seen in the left panel, although this remains to be examined by high-resolution radio observations in the future.

Further discussions regarding the nature of this jet and its impacts to the Red Potato galaxy are presented in Section 5.1.

5. Discussion

5.1. How to maintain the quiescent state of a galaxy at the center of a large cool gas reservoir at $z > 3$

The most intriguing result of this work is the discovery of a passive galaxy, with a stellar mass of about $10^{11} M_{\odot}$ and a SFR at least one dex below the SFMS at $z = 3.25$, right at the center of a large cool gas reservoir traced by Ly α emission. Furthermore, no molecular gas is detected inside the galaxy corresponding to a molecular gas fraction limit of $f_{\text{H}_2} < 0.06$. These two results suggest that either gas accretion from the CGM was significantly reduced over timescales longer than a few hundred Myr or that some process is affecting the conversion of dense gas into the molecular form *within* the galaxy itself.

Important clues to disentangling the different possibilities mentioned above come from a detailed analysis of the properties of the CGM as seen in emission through H α and Ly α . First, the spectral analysis of the Red Potato CGM emission both in Ly α and H α shows broader line profiles than previously measured for CGM emission around AGN. For instance, the Ly α velocity dispersion in a circular annulus between 20 and 30 pkpc from the Red Potato has values between 400 and 500 km/s. This is significantly higher than the velocity dispersion measured for QSO nebulae with similar surface brightness values which range from 50 to 200 km/s within the same circular annuli, as measured by, e.g., González Lobos et al. (2025) and shown in the middle panel of Fig. 8. Since the broadness of the Ly α line could be affected by radiative transfer, a statistical sample of H α spectral profiles for QSO nebulae would be needed to confirm this result, but un-

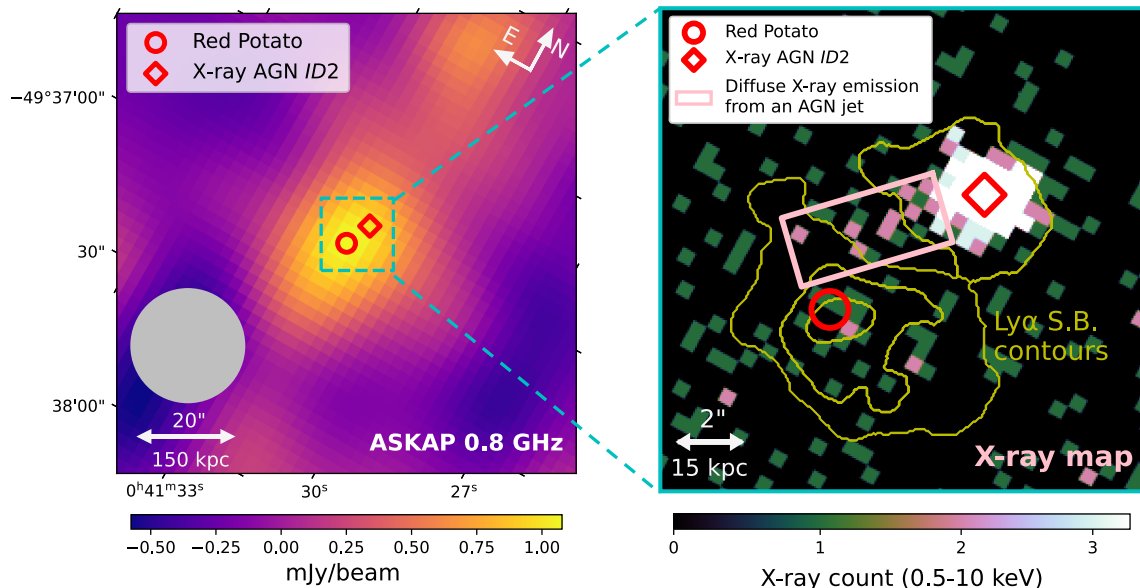


Fig. 10. Analysis of radio and X-ray emission near the Red Potato galaxy. As shown by the map in the left panel, radio emission at 0.8 GHz is detected at significant levels but not spatially resolved, given the ASKAP beam size of around 20 arcsec (gray circle at the lower left corner). The background image in the right panel is a zoomed-in view of the *Chandra* X-ray count map. Diffuse X-ray emission around the AGN neighbor *ID2* is detected and marked by the pink box in the panel, indicating the presence of an X-ray jet which most likely emanates from AGN-*ID2*. The low photon count does not allow a detailed morphological and spectral analysis but the map clearly shows an X-ray photon excess along the direction roughly toward the Red Potato. The Ly α contours from Fig. 1 are also repeated in the right panel for reference. See Sections 4.3 and 5.1.

fortunately such sample is not currently available at $z > 3$ to our knowledge.

However, we note that H α spectral profile in the CGM of the galaxy shows complex and broad kinematics (Figs. 6 & 9), suggesting that the large velocity dispersion measured from the Ly α spectra cannot be solely due to radiative transfer effects but also caused by turbulent gas kinematics.

What could be causing and maintaining an increased turbulence level in the Red Potato's CGM? One possibility could be linked to the previous history of the Red Potato itself, including ejective feedback episodes related to starbursts or AGN activity within the Red Potato which could have depleted its molecular gas reservoir and, at the same time, produced a turbulent CGM. Currently, there is no clear evidence of the presence of an active AGN in the Red Potato from *Chandra* or ALMA observations. At the same time, there is no clear evidence of strong outflows from the Red Potato, either in the form of broad or blueshifted components in [OIII] and CO emission lines or in the form of blueshifted absorption in the Na D lines. As such, although ejective feedback episodes could have initiated the quenching, there is currently no clear evidence that they can maintain the continuous suppression of the Red Potato's star formation despite the presence of the "cold"-gas-rich CGM, over the observed time-scales of a few hundred Myr (Fig. 4).

The deep *Chandra* observations clearly show, instead, that there is a currently active and bright AGN in the vicinity of the Red Potato and present substantial evidence of a jet which emanates from this AGN in the direction of the Red Potato. The presence of a jet is also supported by the ASKAP radio observations which, however, currently lack the resolution to study its detailed morphology. The presence of a jet and its association with AGN-*ID2* thus suggest that this *external* cause could be the most probable agent currently maintaining an increased turbulence level in the Red Potato CGM.

Indeed, radio jets are known to be capable of disturbing and dynamically heating gas surrounding galaxies, at least in the lo-

cal universe, and thus significantly elevate the CGM turbulence (Fabian 2012, Krause 2023 and references therein), leading to a possibly reduced efficiency of gas accretion.

Interestingly, the galaxy associated with AGN-*ID2* is a star-forming galaxy with a stellar mass and SFR consistent with the main sequence at this redshift (see Galbiati et al. 2025). The radio jet is thus apparently not currently affecting the SFR of its host galaxy, as it is often seen at high-redshift where the brightest radio-galaxies are also among the systems with the highest SFR (e.g., the SpiderWeb galaxy; Pentericci et al. 1997, 2000; Miley et al. 2006). This is consistent with the turbulent CGM scenario discussed above, in the plausible case that the AGN-*ID2* jet has an opening angle that is too small to significantly affect the inner CGM of its host galaxy but widens on larger spatial scales where it encounters the CGM of the Red Potato. Such a configuration of radio jets is often seen in local sources (e.g., Brienza et al. 2021, 2025).

5.1.1. Comparing with literature studies

The Red Potato adds to the small yet growing collection of $z \gtrsim 3$ quiescent galaxies discovered in overdense, gas-rich environments (Kalita et al. 2021; Kubo et al. 2021; de Graaff et al. 2025; Umehata et al. 2025b; Pérez-Martínez et al. 2025; Guo et al. 2025). Preventive jet-mode AGN feedback was commonly proposed to explain their existence.

Two of these studies investigated the impacts of such preventive feedback by analyzing the CGM properties in detail. Pérez-González et al. (2025) discovered H α -emitting CGM with high velocity dispersion values of 200–300 km/s around a quiescent galaxy, which agrees with our measured values (§4.1) and indicates the presence of turbulent cool CGM. On the other hand, Guo et al. (2025) discovered a large Ly α -emitting CGM which is centered at a quiescent galaxy and has a steep radial velocity gradient according to the Ly α line profiles. They interpreted

the Ly α velocity gradient as a potential sign of active gas accretion, barring the impacts of resonance scattering on the Ly α profiles (e.g., Verhamme et al. 2006), and further argued that the quenching is most likely due to the impacts of AGN feedback on the galaxy interior rather than the halt of CGM gas accretion. This appears at odds with the findings of this work, reporting no significant gas velocity gradient or signs of gas accretion in the H α kinematics. The cause of this potential discrepancy remains to be investigated with better sample statistics and a more comprehensive analysis of the CGM kinematics using non-resonant emission lines such as H α in the future.

5.2. The diverse evolution pathways of massive galaxies in high-redshift overdense environments

The findings of this work, along with those from recent literature studies, indicate a broad range of star formation and morphological properties among massive galaxies in high-redshift proto-clusters or cosmic web nodes. For example, the target field of this work hosts a high concentration of massive SFGs (Pensabene et al. 2024; Galbiati et al. 2025), including the giant disk Big Wheel (Wang et al. 2025b), and also massive compact quiescent galaxies such as the Red Potato (see also Galbiati et al. in prep.). Although located in the same overdense environment and with similar stellar masses, the physical sizes and SFRs of these two types of galaxies differ by as much as one order of magnitude. Similar diversities have been reported by studies of other overdense fields at $z \gtrsim 3$ (Kalita et al. 2021; Kubo et al. 2021; Venkateshwaran et al. 2024; de Graaff et al. 2025; Umehata et al. 2025a; Pérez-González et al. 2025; Guo et al. 2025).

These findings suggest that massive galaxies in high-redshift overdense environments have diverse physical properties, and yet it remains elusive why such diversity occurs. We showed in this work that one plausible cause responsible for the emergence of quiescent galaxies is the AGN feedback. Nevertheless, follow-up studies are needed to fully resolve this puzzle: progress can be made in the future by investigating *statistical samples* of high-redshift massive galaxies in overdense environments (Galbiati et al. in prep.).

6. Summary & Implications

In this work, we presented the serendipitous discovery of a massive red galaxy ($M_\star \simeq 10^{11} M_\odot$) located in a gas-rich cosmic web node at $z = 3.250$. Surprisingly the galaxy, which we call the “Red Potato,” is quiescent with a SFR at least 1 dex below the SFMS (Section 3), although it is at the center of an 80-kpc reservoir of cool CGM (10^4 – 10^5 K) traced by the extended Ly α emission (Section 4).

In terms of gas inside the galaxy, the Red Potato is poor in molecular and neutral gas according to non-detections of the CO(4–3) and Na D lines, indicating a molecular gas fraction smaller than 10% (Section 3.3). Neither does it have detectable gas outflows (Section 3.4). Rest-frame optical emission lines are detected from the galaxy, which are consistent with being driven by AGN illumination rather than star formation (Section 3.2). The galaxy appears to be a dispersion-dominated system according to the kinematics of ionized gas traced by H α .

In terms of CGM properties, the Red Potato is located at the center of a large reservoir of gas traced by a Ly α halo which is around 80 kpc in diameter at a sensitivity limit of 3×10^{-18} erg/s/cm 2 /arcsec 2 (Section 4.1). In addition, the H α

and [O III] lines are also more spatially extended than the galaxy stellar continuum. The Red Potato CGM shows high velocity dispersion values according to the observed Ly α and H α line profiles, which indicate elevated levels of gas turbulence in the CGM compared to other Ly α nebulae at similar redshifts and Ly α surface brightness values (Section 4.2).

Intriguingly, deep X-ray observations suggest the presence of an extended X-ray jet which most likely emanates from a luminous X-ray AGN neighbor, indicating a certain form of jet-mode feedback acting on the Red Potato CGM. This is corroborated by the detection of bright radio emission in the low-resolution ASKAP 0.8 GHz map (Section 4.3).

Specifically, we argue that the jet feedback may have led to increased CGM turbulence around the Red Potato and thus have reduced the gas accretion onto the galaxy, which is indicated by the high gas velocity dispersion measured from the Ly α and H α line profiles. In addition, the nearby AGN(s) or the large overdensity of AGN associated with the Red Potato environment, may also be illuminating the Red Potato’s cool CGM component, making it visible through fluorescent line emission. The scenario described above is supported by the deep multi-wavelength observations unique to this field (Pensabene et al. 2024; Travascio et al. 2025; Galbiati et al. 2025; Wang et al. 2025b).

Our study demonstrates that the star formation rates of high-redshift galaxies could be substantially reduced and maintained at a low level even within gas-rich and overdense environments in particular situations, such as for galaxies in the vicinity of AGN with active jets.

We emphasize that, in order to fully resolve the puzzle of early-epoch galaxy quenching, future studies need to target not only the galaxies themselves but also their CGM and environment. This work is one of the few studies to date that have probed the CGM of quiescent galaxies at $z > 3$. Future studies utilizing a larger galaxy sample for this purpose would be essential to reveal the quenching pathways of early-epoch galaxies from a statistical perspective.

Acknowledgements. WW would like to thank M. Brienza, C. D’Eugenio, L. di Mascolo, Min Du, F. Fiore, L. Kimmig, P. Oesch, P. Pérez-González, R.-S. Remus, Dongdong Shi, N. Sulzenauer, Tao Wang for insightful discussions related to this work. This project was supported by the European Research Council (ERC) Consolidator Grant 864361 (CosmicWeb). A.P. acknowledges the support from Fondazione Cariplo grant no. 2020-0902. This work is based in part on observations made with the NASA/ESA/CSA James Webb Space Telescope. The data were obtained from the Mikulski Archive for Space Telescopes at the Space Telescope Science Institute, which is operated by the Association of Universities for Research in Astronomy, Inc., under NASA contract NAS 5-03127 for JWST. These observations are associated with program #1835. Support for program #1835 was provided by NASA through a grant from the Space Telescope Science Institute, which is operated by the Association of Universities for Research in Astronomy, Inc., under NASA contract NAS 5-03127. This research is based on observations made with the NASA/ESA Hubble Space Telescope obtained from the Space Telescope Science Institute, which is operated by the Association of Universities for Research in Astronomy, Inc., under NASA contract NAS 5-26555. These observations are associated with program 17065. ALMA is a partnership of ESO (representing its member states), NSF (USA) and NINS (Japan), together with NRC (Canada), MOST and ASIAA (Taiwan), and KASI (Republic of Korea), in cooperation with the Republic of Chile. The Joint ALMA Observatory is operated by ESO, AUI/NRAO and NAOJ. The scientific results reported in this article are based in part on observations made by the *Chandra* X-ray Observatory. This work is also based on observations collected at the European Southern Observatory under ESO programme (110.23ZX).

References

- Afruni, A., Fraternali, F., & Pezzulli, G. 2019, A&A, 625, A11
- Alberts, S. & Noble, A. 2022, Universe, 8, 554
- Alberts, S., Williams, C. C., Helton, J. M., et al. 2024, ApJ, 975, 85

Alexander, P. & Leahy, J. P. 1987, MNRAS, 225, 1

Avery, C. R., Wuyts, S., Förster Schreiber, N. M., et al. 2022, MNRAS, 511, 4223

Baker, W. M., Lim, S., D'Eugenio, F., et al. 2025, MNRAS, 539, 557

Baldwin, J. A., Phillips, M. M., & Terlevich, R. 1981, Publ. Astron. Soc. Pac., 93, 5

Baron, D., Netzer, H., Lutz, D., Prochaska, J. X., & Davies, R. I. 2022, MNRAS, 509, 4457

Belli, S., Park, M., Davies, R. L., et al. 2024, Nature, 630, 54

Bertin, E. & Arnouts, S. 1996, A&AS, 117, 393

Beverage, A. G., Slob, M., Kriek, M., et al. 2025, ApJ, 979, 249

Blumenthal, G. R., Faber, S. M., Primack, J. R., & Rees, M. J. 1984, Nature, 311, 517

Bolatto, A. D., Wolfire, M., & Leroy, A. K. 2013, ARA&A, 51, 207

Boogaard, L. A., van der Werf, P., Weiss, A., et al. 2020, ApJ, 902, 109

Borisova, E., Cantalupo, S., Lilly, S. J., et al. 2016, Astrophys. J., 831, 39

Bradley, L., Sipőcz, B., Robitaille, T., et al. 2024, astropy/photutils: 2.0.2

Brienza, M., Rajpurohit, K., Churazov, E., et al. 2025, A&A, 696, A239

Brienza, M., Shimwell, T. W., De Gasperin, F., et al. 2021, Nature Astronomy, 5, 1261

Calzetti, D. 2001, Publ. Astron. Soc. Pac., 113, 1449

Cantalupo, S. 2017, in Astrophysics and Space Science Library, Vol. 430, Gas Accretion onto Galaxies, ed. A. Fox & R. Davé, 195

Cantalupo, S., Arrigoni Battaia, F., Prochaska, J. X., Hennawi, J. F., & Madau, P. 2014, Nature, 506, 63

Cantalupo, S., Pezzulli, G., Lilly, S. J., et al. 2019, MNRAS, 483, 5188

Cantalupo, S., Porciani, C., Lilly, S. J., & Minati, F. 2005, ApJ, 628, 61

Cappellari, M. 2023, MNRAS, 526, 3273

Carnall, A. C., Cullen, F., McLure, R. J., et al. 2024, MNRAS, 534, 325

Carnall, A. C., McLure, R. J., Dunlop, J. S., et al. 2023, Nature, 619, 716

Chabrier, G. 2003, Publ. Astron. Soc. Pac., 115, 763

Charlot, S. & Fall, S. M. 2000, Astrophys. J., 539, 718

Chiang, Y.-K., Overzier, R. A., Gebhardt, K., & Henriques, B. 2017, ApJ, 844, L23

Conroy, C. & Gunn, J. E. 2010, ApJ, 712, 833

Conroy, C., Gunn, J. E., & White, M. 2009, ApJ, 699, 486

Danhaine, A. L., Tacchella, S., Übler, H., et al. 2025, arXiv e-prints, arXiv:2503.21863

de Graaff, A., Setton, D. J., Brammer, G., et al. 2025, Nature Astronomy, 9, 280

de la Vega, A., Babcock, M. D., Mobasher, B., et al. 2025, arXiv e-prints, arXiv:2501.09066

D'Eugenio, C., Daddi, E., Gobat, R., et al. 2020, ApJ, 892, L2

D'Eugenio, F., Pérez-González, P. G., Maiolino, R., et al. 2024, Nature Astronomy, 8, 1443

Duchesne, S. W., Grundy, J. A., Heald, G. H., et al. 2024, PASA, 41, e003

Elbaz, D., Daddi, E., Le Borgne, D., et al. 2007, A&A, 468, 33

Faber, S. M., Willmer, C. N. A., Wolf, C., et al. 2007, ApJ, 665, 265

Fabian, A. C. 2012, ARA&A, 50, 455

Forrest, B., Lemaux, B. C., Shah, E. A., et al. 2024, ApJ, 971, 169

Forrest, B., Wilson, G., Muzzin, A., et al. 2022, ApJ, 938, 109

Förster Schreiber, N. M. & Wuyts, S. 2020, Annu. Rev. Astron. Astrophys., 58, 661

Fruchter, A. S. & Hook, R. N. 2002, PASP, 114, 144

Gadotti, D. A. 2009, MNRAS, 393, 1531

Galbiati, M., Cantalupo, S., Steidel, C., et al. 2025, A&A, 696, A95

Glazebrook, K., Nanayakkara, T., Schreiber, C., et al. 2024, Nature, 628, 277

Glazebrook, K., Schreiber, C., Labbé, I., et al. 2017, Nature, 544, 71

González Lobos, J., Arrigoni Battaia, F., Obreja, A., et al. 2025, arXiv e-prints, arXiv:2507.16898

Guo, S., Daddi, E., Gobat, R., et al. 2025, arXiv e-prints, arXiv:2510.01421

Hale, C. L., McConnell, D., Thomson, A. J. M., et al. 2021, PASA, 38, e058

Hatch, N. A., Kurk, J. D., Pentericci, L., et al. 2011, MNRAS, 415, 2993

Ilbert, O., McCracken, H. J., Le Fevre, O., et al. 2013, A&A, 556, A55

Ito, K., Tanaka, M., Valentino, F., et al. 2023, ApJ, 945, L9

Ito, K., Valentino, F., Brammer, G., et al. 2024, ApJ, 964, 192

Jiang, F., Liang, J., Jin, B., et al. 2025, arXiv e-prints, arXiv:2504.01070

Jin, S., Sillasen, N. B., Magdis, G. E., et al. 2024, A&A, 683, L4

Johnson, B. D., Leja, J., Conroy, C., & Speagle, J. S. 2021, ApJS, 254, 22

Kakimoto, T., Tanaka, M., Onodera, M., et al. 2024, ApJ, 963, 49

Kalita, B. S., Daddi, E., D'Eugenio, C., et al. 2021, ApJ, 917, L17

Kawinwanichakij, L., Glazebrook, K., Nanayakkara, T., et al. 2025, arXiv e-prints, arXiv:2505.03089

Kennicutt, R. C. & Evans, N. J. 2012, ARA&A, 50, 531

Kereš, D., Katz, N., Weinberg, D. H., & Davé, R. 2005, MNRAS, 363, 2

Kewley, L. J., Dopita, M. A., Sutherland, R. S., Heisler, C. A., & Trevena, J. 2001, Astrophys. J., 556, 121

Koyama, Y., Kodama, T., Tadaki, K.-i., et al. 2013, MNRAS, 428, 1551

Krause, M. G. H. 2023, Galaxies, 11, 29

Kriek, M., Beverage, A. G., Price, S. H., et al. 2024, ApJ, 966, 36

Kubo, M., Umehata, H., Matsuda, Y., et al. 2021, ApJ, 919, 6

Lagos, C. d. P., Valentino, F., Wright, R. J., et al. 2025, MNRAS, 536, 2324

Langen, V., Cantalupo, S., Steidel, C. C., et al. 2023, MNRAS, 519, 5099

Leibler, C. N., Cantalupo, S., Holden, B. P., & Madau, P. 2018, MNRAS, 480, 2094

Leja, J., Carnall, A. C., Johnson, B. D., Conroy, C., & Speagle, J. S. 2019, ApJ, 876, 3

Leja, J., Johnson, B. D., Conroy, C., van Dokkum, P. G., & Byler, N. 2017, ApJ, 837, 170

Mackenzie, R., Pezzulli, G., Cantalupo, S., et al. 2021, MNRAS, 502, 494

Madau, P. & Dickinson, M. 2014, ARA&A, 52, 415

Magdis, G. E., Gobat, R., Valentino, F., et al. 2021, A&A, 647, A33

Man, A. & Belli, S. 2018, Nature Astronomy, 2, 695

Man, A. W. S., Zabl, J., Brammer, G. B., et al. 2021, ApJ, 919, 20

McConachie, I., Wilson, G., Forrest, B., et al. 2025, ApJ, 978, 17

McConnell, D., Hale, C. L., Lenc, E., et al. 2020, PASA, 37, e048

Michałowski, M., Hjorth, J., & Watson, D. 2010, A&A, 514, A67

Miley, G. K., Overzier, R. A., Zirm, A. W., et al. 2006, ApJ, 650, L29

Myers, S. T. & Spangler, S. R. 1985, ApJ, 291, 52

Nanayakkara, T., Esdale, J., Glazebrook, K., et al. 2022, PASA, 39, e002

Noeske, K. G., Weiner, B. J., Faber, S. M., et al. 2007, ApJ, 660, L43

Pacifica, C., Iyer, K. G., Mobasher, B., et al. 2023, Astrophys. J., 944, 141

Park, M., Belli, S., Conroy, C., et al. 2024, ApJ, 976, 72

Pasha, I. & Miller, T. B. 2023, The Journal of Open Source Software, 8, 5703

Pensabene, A., Cantalupo, S., Ciccone, C., et al. 2024, A&A, 684, A119

Pensabene, A., Cantalupo, S., Wang, W., et al. 2025, arXiv e-prints, arXiv:2507.16921

Pentericci, L., Kurk, J. D., Röttgering, H. J. A., et al. 2000, A&A, 361, L25

Pentericci, L., Roettgering, H. J. A., Miley, G. K., Carilli, C. L., & McCarthy, P. 1997, A&A, 326, 580

Pérez-González, P. G., D'Eugenio, F., Rodríguez del Pino, B., et al. 2025, Nature Astronomy [arXiv: 2405.03744]

Pérez-Martínez, J. M., Dannerbauer, H., Emonts, B. H. C., et al. 2025, A&A, 696, A236

Popesso, P., Concas, A., Cresci, G., et al. 2023, Mon. Not. R. Astron., 519, 1526

Roberts-Borsani, G. W. 2020, MNRAS, 494, 4266

Santini, P., Castellano, M., Merlin, E., et al. 2021, A&A, 652, A30

Santini, P., Merlin, E., Fontana, A., et al. 2019, MNRAS, 486, 560

Sato, R. A., Inoue, A. K., Harikane, Y., et al. 2024, MNRAS, 534, 3552

Scholtz, J., D'Eugenio, F., Maiolino, R., et al. 2024, arXiv e-prints, arXiv:2405.19401

Sérsic, J. L. 1963, Bol. Asoc. Argent. Astron. Plata Argent., 6, 41

Setton, D. J., Khullar, G., Miller, T. B., et al. 2024, ApJ, 974, 145

Simons, R. C., Kassin, S. A., Weiner, B. J., et al. 2017, ApJ, 843, 46

Speagle, J. S., Steinhardt, C. L., Capak, P. L., & Silverman, J. D. 2014, Astrophys. J. Suppl. Ser., 214, 15

Steidel, C. C., Adelberger, K. L., Shapley, A. E., et al. 2005, ApJ, 626, 44

Steidel, C. C., Adelberger, K. L., Shapley, A. E., et al. 2000, ApJ, 532, 170

Tacconi, L. J., Genzel, R., Saintonge, A., et al. 2018, ApJ, 853, 179

Tacconi, L. J., Genzel, R., & Sternberg, A. 2020, ARA&A, 58, 157

Tanaka, M., Onodera, M., Shimakawa, R., et al. 2024, ApJ, 970, 59

Travascio, A., Cantalupo, S., Tozzi, P., et al. 2025, A&A, 694, A165

Umehata, H., Kubo, M., & Nakaniishi, K. 2025a, ApJ, 985, L8

Umehata, H., Steidel, C. C., Smail, I., et al. 2025b, PASJ, 77, 432

Valentino, F., Brammer, G., Gould, K. M. L., et al. 2023, ApJ, 947, 20

Valentino, F., Heintz, K. E., Brammer, G., et al. 2025, arXiv e-prints, arXiv:2503.01990

Valentino, F., Tanaka, M., Davidzon, I., et al. 2020, ApJ, 889, 93

van de Sande, J., Kriek, M., Franx, M., et al. 2013, ApJ, 771, 85

Vazdekis, A., Sánchez-Blázquez, P., Falcón-Barroso, J., et al. 2010, MNRAS, 404, 1639

Veilleux, S., Cecil, G., & Bland-Hawthorn, J. 2005, ARA&A, 43, 769

Venkateswaran, A., Weiss, A., Sulzenauer, N., et al. 2024, ApJ, 977, 161

Verhamme, A., Schaerer, D., & Maselli, A. 2006, A&A, 460, 397

Wang, B., Leja, J., Labbé, I., et al. 2024, ApJS, 270, 12

Wang, G. C. P., Chapman, S. C., Sulzenauer, N., et al. 2025a, ApJ, 983, 69

Wang, W., Cantalupo, S., Pensabene, A., et al. 2025b, Nature Astronomy, 9, 710

Wang, X., Cantalupo, S., Wang, W., et al. 2025c, arXiv e-prints, arXiv:2511.19608

Weibel, A., de Graaff, A., Setton, D. J., et al. 2025, ApJ, 983, 11

Wisnioski, E., Mendel, J. T., Leaman, R., et al. 2025, arXiv e-prints, arXiv:2505.24129

Witten, C., Oesch, P. A., McClymont, W., et al. 2025, arXiv e-prints, arXiv:2507.06284

Wu, P.-F. 2025, ApJ, 978, 131

Yang, L., Kartaltepe, J. S., Franco, M., et al. 2025, arXiv e-prints, arXiv:2504.07185

Zhou, D., Chapman, S. C., Sulzenauer, N., et al. 2025a, ApJ, 982, L17

Zhou, L., Wang, T., Daddi, E., et al. 2025b, arXiv e-prints, arXiv:2507.09971

Appendix A: Flux Calibration of the NIRSpec Spectrum

The NIRSpec slit has a width of $0.2''$, significantly smaller than the spatial extent of the Red Potato galaxy. The loss of flux out of the slit leads to an overall lower flux level of the NIRSpec spectrum, compared to the total fluxes measured from the photometric filters covering the same wavelength range. To address this, we first conduct a PROSPECTOR run using only the multi-band photometric data, with other setups identical to those described in Section 3.2, and obtained a best-fit model spectrum from the fitting, which is shown as the gray curve in the middle panel of Fig. A.1. Then, this model spectrum was compared with the observed NIRSpec spectrum (thick goldenrod curve) to obtain a wavelength-dependent flux correction factor: the ratio between the former and latter was fit as a fifth-order polynomial of the wavelength, leading to a correction factor presented in the lower panel of the figure. An outlier clipping step was implemented in the process to avoid the impact of the misfit emission lines, which were unconstrained in the photometry-only SED fitting. The resulting factor, overall increasing with the wavelength, was multiplied onto the NIRSpec spectrum to account for the flux loss, before it was used for the SED fitting in Section 3.2.

[In addition, we also assess the impacts of adopting a different form of SFH and adding the NIRSpec spectrum to the fitting, which are demonstrated in Fig. A.2.]

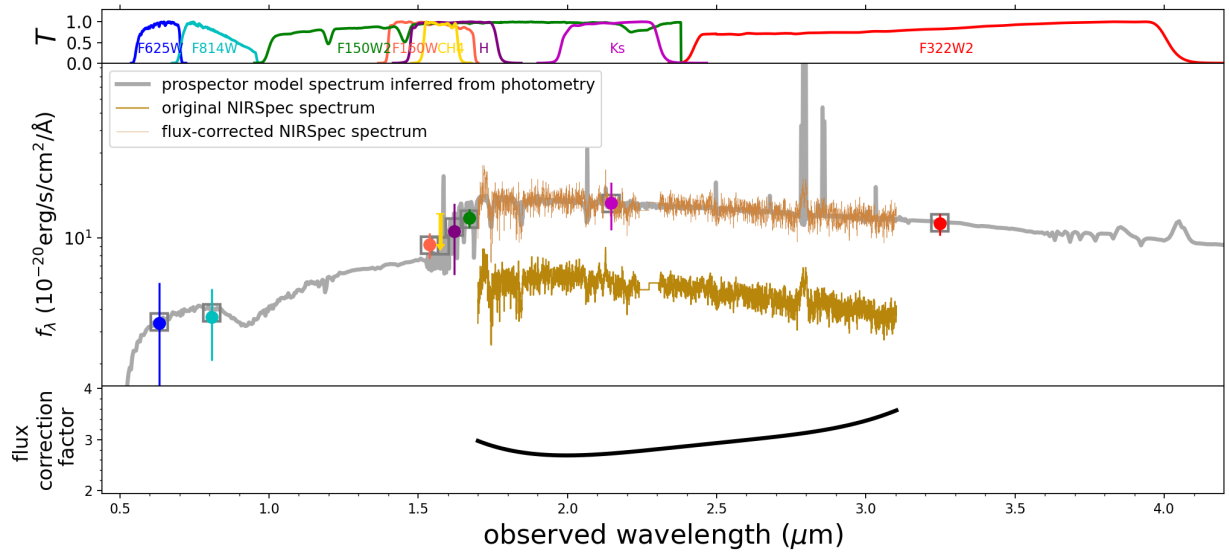


Fig. A.1. Correction of the slit flux loss to the observed NIRSpec spectrum. The observed spectrum (thick goldenrod curve) has an overall lower flux level compared to the total photometric fluxes (filled circles) because the slit does not cover the entire galaxy. To correct for this, a model spectrum (gray curve) was obtained from an SED fitting of only the multiband photometric fluxes. The ratio between the model spectrum and observed spectrum excluding the emission line regions is fit as a fifth-order polynomial of the wavelength, leading to a wavelength-dependent factor presented in the lower panel. This factor was applied to the observed NIRSpec spectrum before it was used for the SED fitting in Section 3.2.

Fig. A.2. Comparing the SFHs inferred from different setups of SED fitting, in multiple panels. TBA.

Appendix B: NIRCam Image Sérsic fitting results

The galaxy images in the two NIRCam filters, F150W2 (rest-frame $0.4\ \mu\text{m}$) and F322W2 (rest-frame $0.8\ \mu\text{m}$), were fit with 2D Sérsic profiles with pysersic (Pasha & Miller 2023). The images and best-fit models are presented in the left and middle panels of Fig. B.1. The NIRCam PSF was taken into account in the fitting, and a mask was placed near the upper left corner of the image to mask out a separate object projected on the sky. Other details of the fitting setup can be found in Wang et al. (2025b). According to the fitting results, the galaxy is compact in both filters, with half-light radii of 0.13 and 0.11 arcsec and Sérsic indices of 1.5 and 2.6 for F150W2 and F322W2, respectively.

The residual images are also shown in the right panels, where small objects are found near the Red Potato galaxy. However, without the coverage from the JWST spectroscopic observations, the redshifts of these neighbors cannot be determined. At the galaxy center, no point source is found from the residual map of either filter, indicating that the central AGN of the galaxy (if there exists one) does not have any noticeable continuum emission in the rest-frame UV/optical.

Appendix C: ASKAP Radio Maps

As shown in the left panel of Fig. C.1, the Red Potato galaxy has a radio counterpart detected in 0.8 GHz, the center of which overlaps with the location of the galaxy, indicating a certain form of radio feedback in action. The radio source has a measured flux of 1.56 ± 0.47 mJy, the brightest of the large-scale structure. No significant detection was found in the 1.4 GHz map 2σ limit of

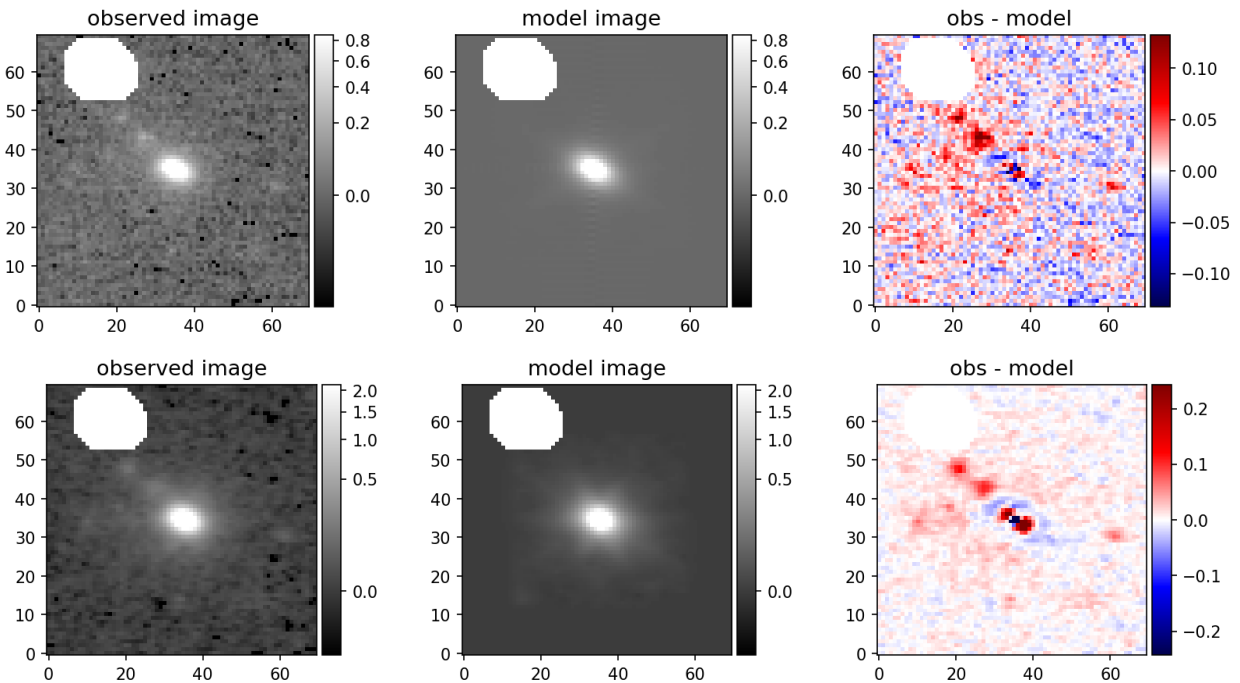


Fig. B.1. Galaxy images (left) and the best-fit Sérsic models (middle), for the F150W2 (rest-frame $0.4 \mu\text{m}$; top row) and F322W2 filters (rest-frame $0.8 \mu\text{m}$; bottom row). The Red Potato galaxy is compact in both filters, with best-fit half-light radii of 0.13 and 0.11 arcsec, respectively, and Sérsic indices below 3. The residual images of the fitting are shown in the right panels.

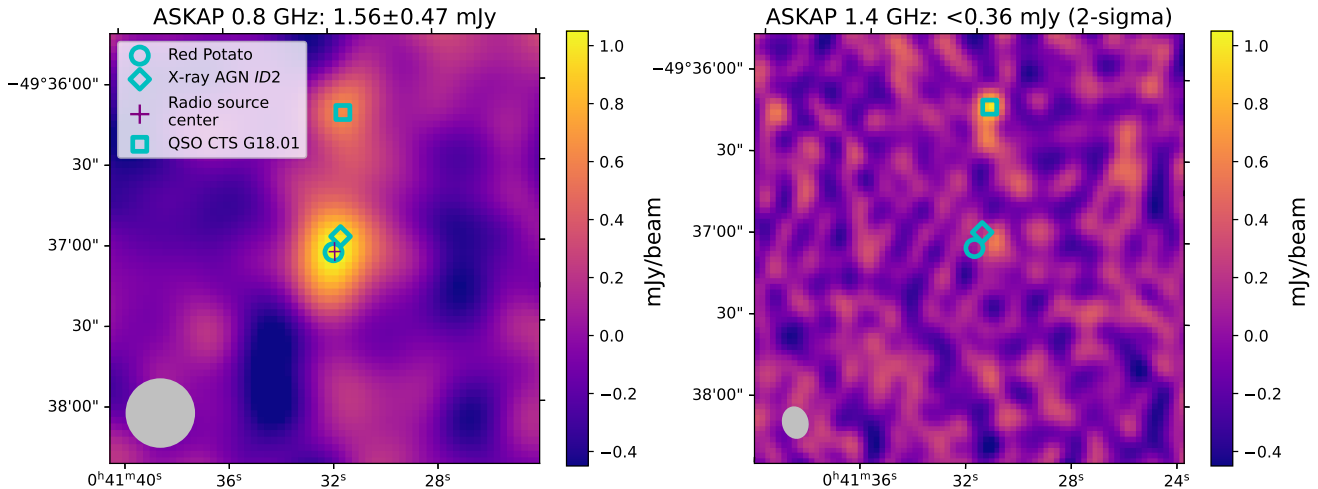


Fig. C.1. ASKAP radio maps. *Left:* The Red Potato galaxy has a radio counterpart in 0.8 GHz, suggesting a certain form of jet-mode feedback in action. The source centroid is marked with the cross symbol. *Right:* This radio source is yet not detected in 1.4 GHz, suggesting a steep radio power law index, which is likely due to the aging of a jet. The ellipse at the lower left corner of each panel represents the ASKAP beam size. Locations of the X-ray AGN neighbor *ID2* are also indicated in both panels.

0.36 mJy; right panel) which, along with the 0.8 GHz detection, indicates a steep radio spectral index (Section 4.3). On the 0.8 GHz map, the radio source appears elongated in a direction slightly offset from north-south, compared to the shape of the ASKAP beam shown in the lower left corner of the left panel. Because the full beam size of the ASKAP map is as large as 20 arcsec, it remains difficult to examine the radio morphology. Higher resolution follow-up radio observations are needed to pinpoint the origin of the radio emission.